Volume 14
Number 24
23 April 2026
Pages 14653–15486

Journal of Materials Chemistry A

Materials for energy and sustainability

rsc.li/materials-a

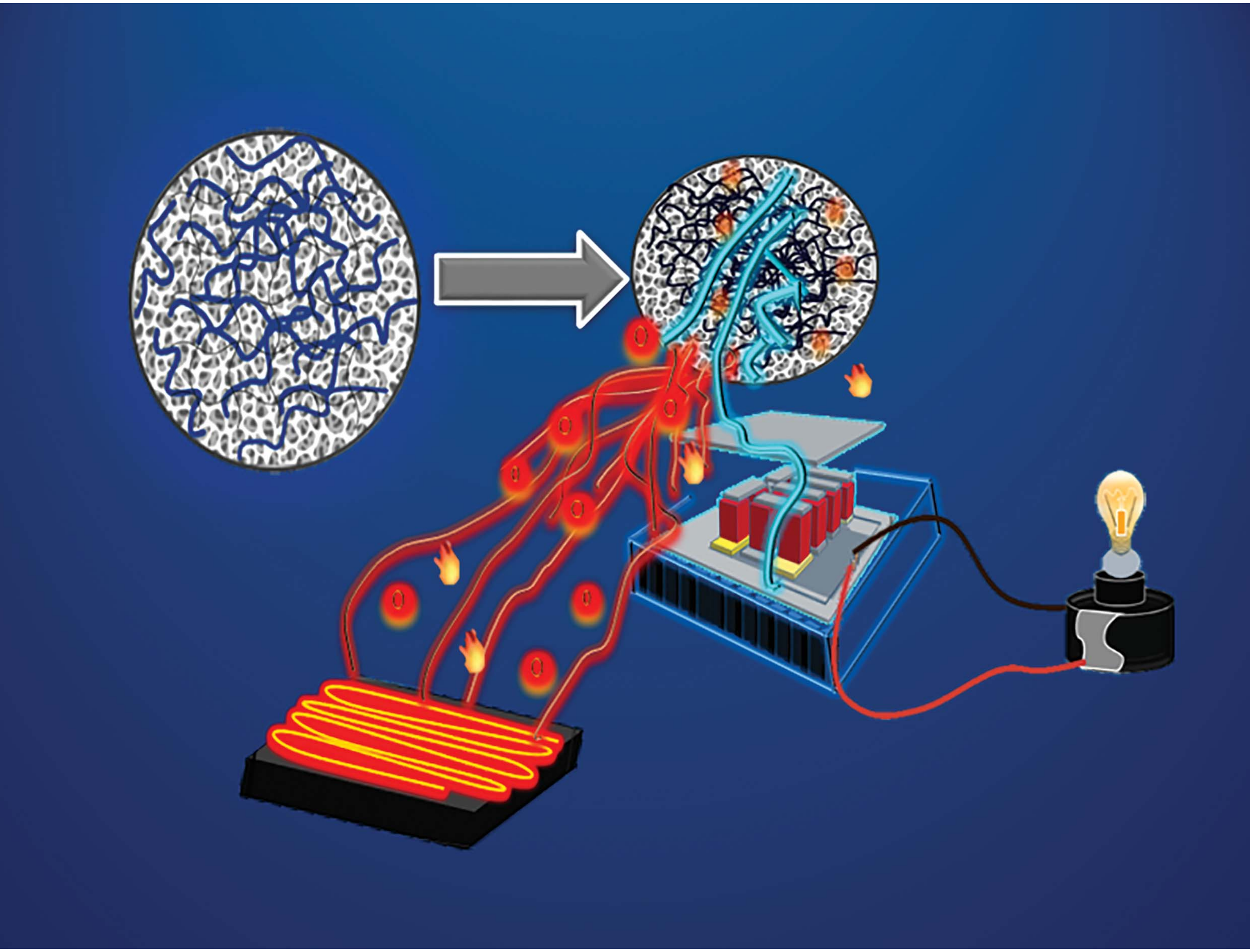

ISSN 2050-7488

ROYAL SOCIETY OF CHEMISTRY

PAPER

Chia-Jyi Liu *et al.*

Indium-filled skutterudite/PEDOT:PSS-derived sulfur-amorphous carbon hybrids: an organic–inorganic interface design strategy for phonon-charge decoupling and enhanced thermoelectric performance

Journal of
Materials Chemistry A

PAPER

View Article Online
View Journal | View Issue

Cite this: *J. Mater. Chem. A*, 2026, **14**, 14884

Indium-filled skutterudite/PEDOT:PSS-derived sulfur-amorphous carbon hybrids: an organic–inorganic interface design strategy for phonon-charge decoupling and enhanced thermoelectric performance

Vinothkumar Lourdhusamy,[a] Immanuel Paulraj,[a] Veera Prabu Kannan,[b] Niranjan A.S.[a] and Chia-Jyi Liu*[a]

Reducing lattice thermal conductivity (κ_L) in filled skutterudites while preserving power factor remains a central challenge for mid-temperature waste-heat recovery. Here, we introduce an interphase-directed strategy in which HNO_3-treated PEDOT:PSS, co-processed with In-filled Co_4Sb_{12}, undergoes an *in situ* polymer-to-sulfur-doped amorphous carbon (S-AC) conversion. The resulting ultrathin S-AC interlayers construct a hierarchical micro/mesoporous network that reshapes phonon transport through diffuse boundary scattering, acoustic-impedance mismatch, and multiphase strain-field perturbations. These interface-dominated processes produce a pronounced suppression of κ_L beyond what is typically associated with porosity alone in skutterudites. A Kane-model Lorenz analysis further reveals a composition-dependent balance in electronic transport: moderate S-AC loadings improve mobility *via* intergranular bridging, whereas high interphase density introduces extensive carrier scattering that lowers κ_e and contributes to the minimum total κ. The optimized hybrid achieves $\kappa \approx 0.74$ W m^{-1} K^{-1} and $zT = 1.47$ at 700 K. A 10-pair module, pairing this n-type leg with $Mg_2Zn_{0.97}Ag_{0.03}Sb_2$, delivers 203.32 μW cm^{-2} and 5.53% efficiency at $\Delta T = 160$ K, demonstrating device-level viability. This interphase-engineering concept provides a scalable and composition-agnostic route to strong κ_L suppression while maintaining favorable electronic transport, offering a broadly applicable design framework for next-generation mid-temperature thermoelectrics.

Received 24th January 2026
Accepted 24th March 2026

DOI: 10.1039/d6ta00685j

rsc.li/materials-a

1. Introduction

With the current energy infrastructure's inadequacy in meeting rising energy demands, and under growing scrutiny due to environmental concerns contributing to climate change, a shift towards sustainable and efficient energy sources has become a necessity.[1] Among the various alternatives, thermoelectric (TE) devices provide a sustainable approach for the direct conversion of heat into electricity. The efficiency of TE materials is quantified by a dimensionless parameter, known as the dimensionless figure of merit (zT), defined as: $zT = S^2\sigma T/\kappa$, where $\kappa = \kappa_L + \kappa_e$.[2] Achieving high zT requires simultaneously maximizing the power factor $S^2\sigma$ and minimizing the lattice thermal conductivity κ_L. Over the past few decades, diverse material systems such as PbTe,[3] SnTe,[4] GeTe,[5] SnSe,[6] Half-Heusler alloys,[7] Zintl compounds,[8,9] filled skutterudites,[2] and organic-inorganic hybrid composites[10] have been extensively explored for mid-temperature TE applications. However, challenges including toxicity, scarcity of constituent elements, and limited material sustainability have hindered their large-scale deployment.

Among mid-temperature thermoelectric materials, $CoSb_3$-based skutterudites (commonly written as Co_4Sb_{12} for the full cell) are notable for its excellent transport properties, low cost, and elemental abundance.[11–13] Throughout this work, we use $CoSb_3$ to denote the parent framework; specific compositions are reported on the Co_4Sb_{12} cell (*e.g.*, $In_{0.032}Co_{3.6}Ni_{0.28}Fe_{0.12}Sb_{12}$). They crystallize in a cubic structure, $Im\bar{3}$ (No. 204), featuring two intrinsic voids that can host "rattler" atoms to scatter phonons and reduce lattice thermal conductivity (κ_L).[14] $CoSb_3$ also offers high carrier mobility and a large Seebeck coefficient, ideal for operation between 500–800 K. However, a practical strategy for strongly suppressing the lattice thermal conductivity beyond what is expected from porosity dilution alone, while simultaneously preserving a high power factor and device-level viability, remains an open challenge. Extensive efforts have tuned $CoSb_3$ *via* alloying, filling, and stoichiometry control, tailoring carrier concentration/band structure and reducing κ_L,[15–17] enhance effective mass,[18,19] and suppress κ_L *via* multiscale phonon scattering.[20–23] Notably, Li *et al.*[20] achieved zT

---

[a] *Department of Physics, National Changhua University of Education, Changhua 500, Taiwan. E-mail: liucj@cc.ncue.edu.tw*

[b] *Department of Metallurgical and Materials Engineering, IIT Madras, Chennai 600036, Tamil Nadu, India*

$\approx$ 1 at >750 K in partially Yb-filled Co_4Sb_{12}. Gharleghi *et al.*[24] obtained $zT = 1.0$ at 575 K for $In_{0.04}Co_4Sb_{12}$–$InSb_{0.05}$ nanocomposites, and later explored Ni–Fe co-doped $Co_{4-y-z}Ni_xFe_ySb_{12}$, *via* In incorporation.[24,25]

Suppressing the lattice thermal conductivity (κ_L) is a key strategy for improving the thermoelectric performance of Co_4Sb_{12} while maintaining a high power factor. Beyond alloying and nanostructuring, porosity engineering provides an effective route to enhance phonon scattering by introducing voids that disrupt phonon mean free paths and reduce the effective thermal conductivity. Organic–inorganic hybridization can further amplify this effect, as polymer-derived phases generate micro-/mesopores and heterogeneous interfaces that act as additional phonon-scattering centers. For example, Jung *et al.*[26] demonstrated that incorporating porous PDMS into Bi_2Te_3 reduced κ to ~0.08 W m^{-1} K^{-1} while preserving favorable electronic transport, highlighting the effectiveness of hybrid interface design.

To quantitatively evaluate whether κ_L reduction can be explained solely by porosity, this work adopts two standard two-phase effective-medium theory (EMT) models—the Maxwell–Eucken model and the Bruggeman self-consistent approximation—as conservative porosity-only baselines. In these formulations, κ_s and κ_p denote the lattice thermal conductivities of the continuous skutterudite matrix and dispersed pore phase, respectively. Because the pores are predominantly air-filled or vacuum-like, κ_p is expected to be negligible compared with κ_s; accordingly, $\kappa_p \approx 0$ W m^{-1} K^{-1} is adopted as the primary baseline, and $\kappa_p = 0.05$ W m^{-1} K^{-1} is additionally evaluated as a sensitivity case to ensure robustness of the EMT comparison (Section 3.6.1). These parameter-free EMT models provide reference predictions based solely on phase thermal conductivities and volume fractions, enabling direct quantitative comparison between experimental κ_L and porosity-only expectations.

Here we advance an interface-engineering strategy that couples indium filling with HNO_3-treated PEDOT:PSS-derived sulfur-doped amorphous carbon (S-AC). The concept is twofold: (i) indium filling optimizes carrier concentration while preserving mobility, and (ii) the polymer-derived phase forms a low-thermal-conductivity, interface-dense network that enhances phonon scattering while simultaneously providing conductive bridges across grain boundaries. We prepare $In_{0.032}Co_{3.6}Ni_{0.28}Fe_{0.12}Sb_{12}/x$ wt% PEDOT:PSS/S-AC composites ($x = 10$–40) and examine their structure-transport relationships over 325–700 K. During co-processing at 580 °C, HNO_3-treated PEDOT:PSS undergoes *in situ* conversion into sulfur-doped amorphous-carbon interlayers, generating a hierarchical micro/mesoporous network throughout the skutterudite matrix. This interphase network enhances diffuse phonon scattering through boundary roughness, acoustic impedance mismatch, and multiphase structural disorder while preserving intergranular electronic connectivity.

Using the Maxwell–Eucken and Bruggeman porosity-only EMT baselines defined above, the experimentally measured κ_L of the 40 wt% composite is found to be lower than the model predictions at 325 K and 700 K (approximately 16–22%, depending on model and κ_p assumption; see Section 3.6.1), while achieving $\kappa \approx 0.74$ W m^{-1} K^{-1} and $zT = 1.47$ at 700 K. A 10-pair thermoelectric module further demonstrates device compatibility at $\Delta T = 160$ K. These results indicate that interface-mediated phonon scattering arising from amorphous interphases, multiphase inclusions, and hierarchical microstructural disorder contributes significantly beyond porosity dilution alone.

Building on our prior demonstration of *in situ* polymer-derived interphase formation in thermoelectric composites,[27–29] this work establishes a quantitatively benchmarked interface-engineering strategy for filled skutterudites, combining EMT-referenced thermal transport analysis with Kane-band separation of κ_e and device-level validation.

2. Experimental

2.1 Materials

Cobalt(II) chloride hexahydrate ($CoCl_2\cdot6H_2O$, 95%), nickel(II) chloride hexahydrate ($NiCl_2\cdot6H_2O$, 96%), iron(III) chloride hexahydrate ($FeCl_3\cdot6H_2O$, 97%), antimony (Sb) powder (99.5%), and PEDOT:PSS (PH1000) dispersion was supplied by Uni-Region Bio Tech, and nitric acid (HNO_3) was obtained from DAEJUNG.

2.2 Synthesis of $Co_{3.6}Ni_{0.28}Fe_{0.12}Sb_{12}$

$Co_{3.6}Ni_{0.28}Fe_{0.12}Sb_{12}$ skutterudites were synthesized *via* a hydrothermal route. Quantitatively weighed $CoCl_2\cdot6H_2O$, $NiCl_2\cdot6H_2O$, and $FeCl_3\cdot6H_2O$ were dissolved in 110 mL of reverse osmosis (RO) water inside a Teflon-lined autoclave. The molar ratio of Sb to the total transition metals (Co + Ni + Fe) was maintained at 3 : 1. The detailed hydrothermal synthesis parameters follow those reported in ref. 2 and 30. The resulting powders were vacuum-dried overnight, uniaxially pressed into pellets, and sealed in evacuated Pyrex tubes (10^{-5}–10^{-6} Torr). Sintering was performed at 580 °C for 6 h.

2.3 Fabrication of In-filled $Co_{3.6}Ni_{0.28}Fe_{0.12}Sb_{12}/HNO_3$-treated PEDOT:PSS composites

PEDOT:PSS were post-treated with HNO_3 for 2 min at room temperature to partially remove excess PSS. The treated PEDOT:PSS was rinsed five times with RO water and once with ethanol to eliminate residual acid and impurities, then dried at ambient temperature. The dried polymer (10, 20, and 40 wt%) was mechanically blended with $Co_{3.6}Ni_{0.28}Fe_{0.12}Sb_{12}$ powders to form homogeneous mixtures. Indium filling was carried out by solid-vapor reaction: the composite powders were sealed with a predetermined amount of indium in evacuated Pyrex tubes and annealed at 580 °C for 24 h, enabling indium incorporation into the Sb icosahedral voids of the skutterudite lattice. Schematic representation of the synthesis procedure is shown in Fig. 1.

2.4 Characterization

Phase identification was performed by X-ray diffraction (XRD, Shimadzu XRD-6000) using Fe Kα radiation over a 2θ range of 10–90° with a step size of 0.02°. Bulk density was determined *via* Archimedes' method. X-ray photoemission spectroscopy (XPS)

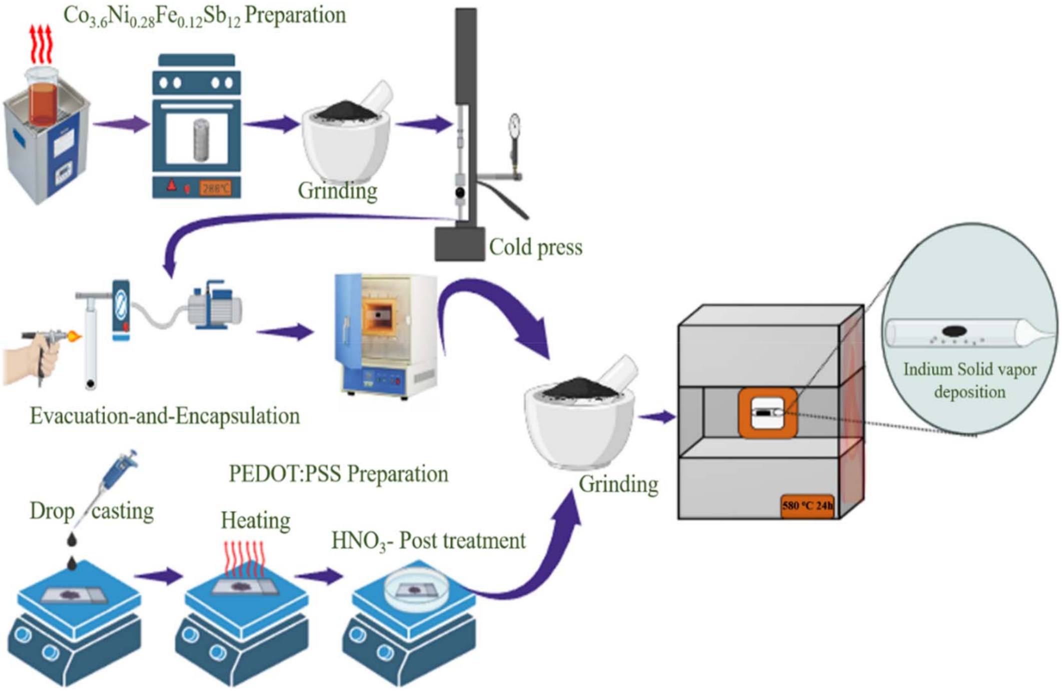

Fig. 1 Schematic diagram of the synthesis workflow for pristine $Co_{3.6}Ni_{0.28}Fe_{0.12}Sb_{12}$ and $In_{0.032}Co_{3.6}Ni_{0.28}Fe_{0.12}Sb_{12}$/PEDOT:PSS/S-AC composites with 10, 20, and 40 wt% HNO_3-treated PEDOT:PSS, sintered at 853 K for 24 h.

was obtained through PHI Hybrid Quantera. High-resolution transmission electron microscopy (HRTEM) images were captured using a JEOL JEM-2010 (Japan) transmission electron microscope. The vibrational and structural properties of the samples were analyzed using Raman microscopy under an excitation wavelength of 785 nm (Thermo Scientific, USA). Hall effect measurements were conducted at 325 K using the van der Pauw method under a 0.6 T magnetic field. Field-emission scanning electron microscopy (FE-SEM, JEOL JSM-7610F) was used to study the morphology. Temperature dependence of the electrical resistivity and Seebeck coefficient were measured using a Setaram SeebeckPro system, while thermal diffusivity (*D*) was determined *via* a Laser Flash Analyzer (LFA) using LFA-27 (NETZSCH) in a flowing argon atmosphere. The uncertainties in electrical resistivity, Seebeck coefficient, and thermal conductivity measurements were ±10%, ±7%, and ±5%, respectively.

The porosity ϕ in Table 1 (converted from the relative density) is also used in subsequent porosity-only EMT baseline calculations using the Maxwell–Eucken and Bruggeman models (see Section 3.6.1 and Table S1), to quantitatively assess whether κ_L falls below what would be expected from pore-dilution alone.

3. Results and discussion

3.1 Crystallographic structure, refinement and lattice distortion from XRD

Fig. 2(a) presents the X-ray diffraction (XRD) patterns of pristine $Co_{3.6}Ni_{0.28}Fe_{0.12}Sb_{12}$ and $In_{0.032}Co_{3.6}Ni_{0.28}Fe_{0.12}Sb_{12}/x$ wt% HNO_3-treated PEDOT:PSS/S-AC composites, ($x = 10$, 20, and 40). The dominant diffraction peaks correspond to the standard skutterudite Co_4Sb_{12} phase with an $Im\bar{3}$ space group (ICDD #78-0976).[31] In addition to the primary skutterudite reflections, secondary peaks corresponding to elemental Sb, InSb, and In_2O_3 were identified. Sb appears as a minor impurity phase in all samples, while InSb is present in all indium-containing compositions except the pristine skutterudite. A small amount of In_2O_3 is detected only in the 10 wt% composite; at higher PEDOT:PSS loadings its reflections fall below the XRD detection limit. The presence of InSb and In_2O_3 is consistent with

Table 1 Relative density, porosity, and Rietveld refinement results for pristine and composite $Co_{3.6}Ni_{0.28}Fe_{0.12}Sb_{12}$ samples. Composites contain $In_{0.032}Co_{3.6}Ni_{0.28}Fe_{0.12}Sb_{12}$ and x wt% PEDOT:PSS/S-AC ($x = 10$, 20, 40)

	Cubic, (space group) $Im\bar{3}$				
Crystal system	$Co_{3.6}Ni_{0.28}Fe_{0.12}Sb_{12}$ and $In_{0.032}Co_{3.6}Ni_{0.28}Fe_{0.12}Sb_{12}/x$ wt% PEDOT:PSS/S-AC	$x = 0.00$	$x = 10$	$x = 20$	$x = 40$
Lattice parameter	a (Å)	9.0422 (7)	9.0492 (6)	9.0514 (5)	9.0522 (1)
Relative density	ρ_{Bulk}/ρ_{XRD} (%)	84.16	84.87	80.10	73.52
Porosity	∅ (%)	15.84	15.13	19.90	26.48

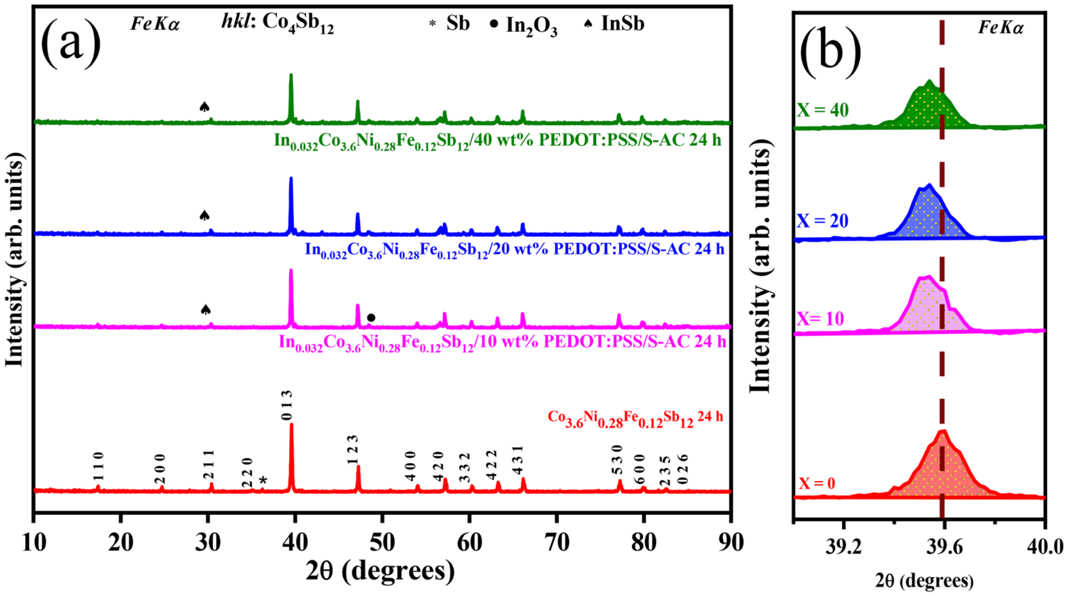

Fig. 2 XRD patterns of (a) pristine $Co_{3.6}Ni_{0.28}Fe_{0.12}Sb_{12}$ and $In_{0.032}Co_{3.6}Ni_{0.28}Fe_{0.12}Sb_{12}$/PEDOT:PSS/S-AC composites with 10, 20, and 40 wt% HNO_3-treated PEDOT:PSS/S-AC and (b) magnified view of the primary peaks.

previous reports,[32,33] where indium incorporation into Co_4Sb_{12} results in either partial substitution at Sb sites or secondary phase formation, depending on synthesis and heat-treatment parameters. It should be noted that both Sb and InSb phases are observed in all composites; however, increasing PEDOT:PSS/S-AC content gradually suppresses the Sb phase while enhancing the relative intensity of InSb reflections. This trend indicates that PEDOT:PSS/S-AC affects phase evolution during sintering, moderating Sb precipitation and promoting InSb formation. Furthermore, Rietveld refinement shows that the lattice parameter increases from 9.0422(7) Å to 9.0522(1) Å with polymer content (Tables 1 and S1); the position of the primary peak in Fig. 2(b) is consistent with this trend. We ascribe the small expansion to strain associated with PEDOT:PSS-derived (S-AC) interphases rather than to any crystalline C or S phase, which are below the XRD detection limit.

Fig. S1 presents the Rietveld refinement of the XRD data, performed using HighScore Xpert to extract lattice parameters and quantify phase fractions, as summarized in Tables 1 and S1. Although PEDOT:PSS is known to decompose above ∼252 ° C, releasing residual carbon- and sulfur-containing species, the refinement results reveal no crystalline C or S phases. This absence suggests that these elements, if present, exist in an amorphous or highly disordered state below the XRD detection limit. Consequently, a detailed investigation of carbon and sulfur distribution was conducted using high-resolution transmission electron microscopy (HRTEM), as discussed subsequently. A systematic decrease in both bulk and XRD densities is observed with increasing PEDOT:PSS content (10, 20, and 40 wt%). Porosity (∅) is calculated from the measured bulk density (ρ_{Bulk}) and crystallographic density (ρ_{XRD}) *via*[34]

$$\varnothing\% = \left(1 - \frac{\rho_{\mathrm{Bulk}}}{\rho_{\mathrm{XRD}}}\right) \times 100 \tag{1}$$

The resulting porosity values are 15.83%, 15.12%, 19.89%, and 26.47% for pristine, 10, 20, and 40 wt% samples, respectively. The porosity increases with a higher content of HNO_3-treated PEDOT:PSS/S-AC, attributed to the introduction of the polymer into the composite matrix, while elevated porosity can act as phonon scattering centers, potentially reducing lattice thermal conductivity but at the expense of electrical transport properties.

3.2 Surface chemical states (XPS)

The high-resolution XPS spectra of the composite are presented in Fig. 3, revealing the presence of Fe, Co, Ni, In, Sb, S, C, and O, thereby confirms the formation of the multicomponent composite. The Fe 2p spectrum Fig. 3(a) exhibits two main peaks located at approximately 710.0 and 724.0 eV, corresponding to the Fe $2p_{3/2}$ and Fe $2p_{1/2}$ states, respectively. Deconvolution indicates the coexistence of Fe^{2+} and Fe^{3+} species together with characteristic shake-up satellite features, suggesting mixed valence states of iron in the material.

The Co 2p spectrum Fig. 3(b) displays two principal peaks centered at approximately 781.8 and 796.7 eV, assigned to Co $2p_{3/2}$ and Co $2p_{1/2}$, respectively. The fitted components at 781.1 and 785.3 eV correspond to the Co $2p_{3/2}$ state, while the remaining peaks originate from the Co $2p_{1/2}$ component. In addition, two pronounced shake-up satellite peaks located at approximately 789.2 and 802.2 eV are observed, confirming the coexistence of Co^{2+} and Co^{3+} oxidation states in the composite.[35]

The Ni 2p spectrum Fig. 3(c) can be deconvoluted into two spin–orbit doublets accompanied by shake-up satellite features. The peaks at 851.18 and 868.44 eV correspond to the Ni^{2+} $2p_{3/2}$ and Ni^{2+} $2p_{1/2}$ states, whereas the peaks at 854.13 and 871.88 eV are attributed to Ni^{3+} $2p_{3/2}$ and Ni^{3+} $2p_{1/2}$ states, respectively. The presence of these satellite features further confirms the characteristic electronic structure of nickel species in the composite.[36]

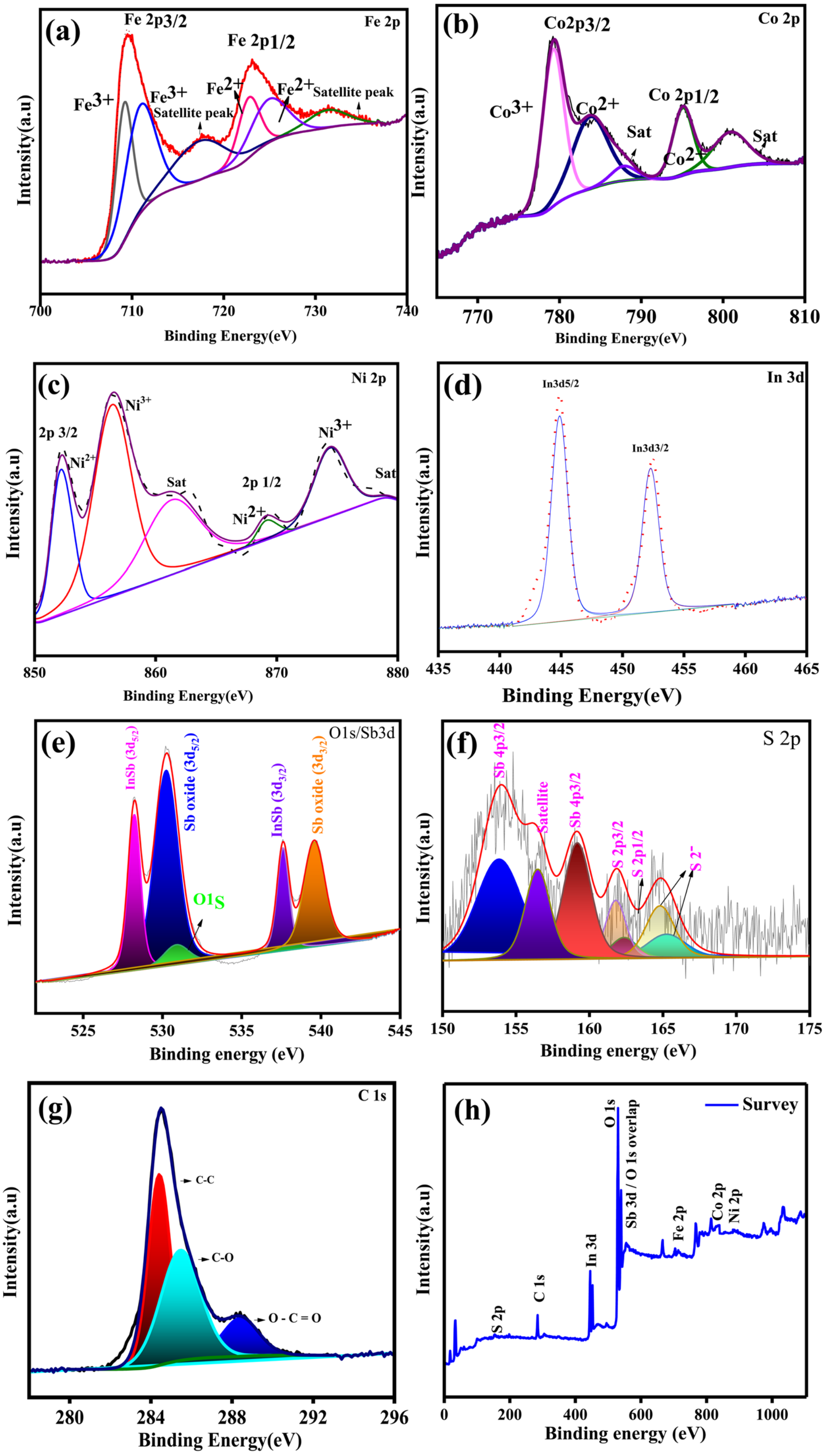

Fig. 3 High-resolution XPS spectra of the composite, showing the deconvoluted core-level spectra of (a) Fe 2p, (b) Co 2p, (c) Ni 2p, (d) In 3d, (e) Sb 3d/O 1s region, (f) S 2p, and (g) C 1s. (h) Survey spectrum of the composite, indicating the presence of all constituent elements.

The In 3d spectrum Fig. 3(d) shows two distinct peaks at approximately 444.5 and 452.1 eV, corresponding to the In $3d_{5/2}$ and In $3d_{3/2}$ states, confirming the presence of indium in the composite.[37] The Sb 3d region Fig. 3(e) exhibits characteristic Sb $3d_{5/2}$ and Sb $3d_{3/2}$ peaks that partially overlap with the O 1s signal, indicating the presence of surface Sb oxide species.[38,39]

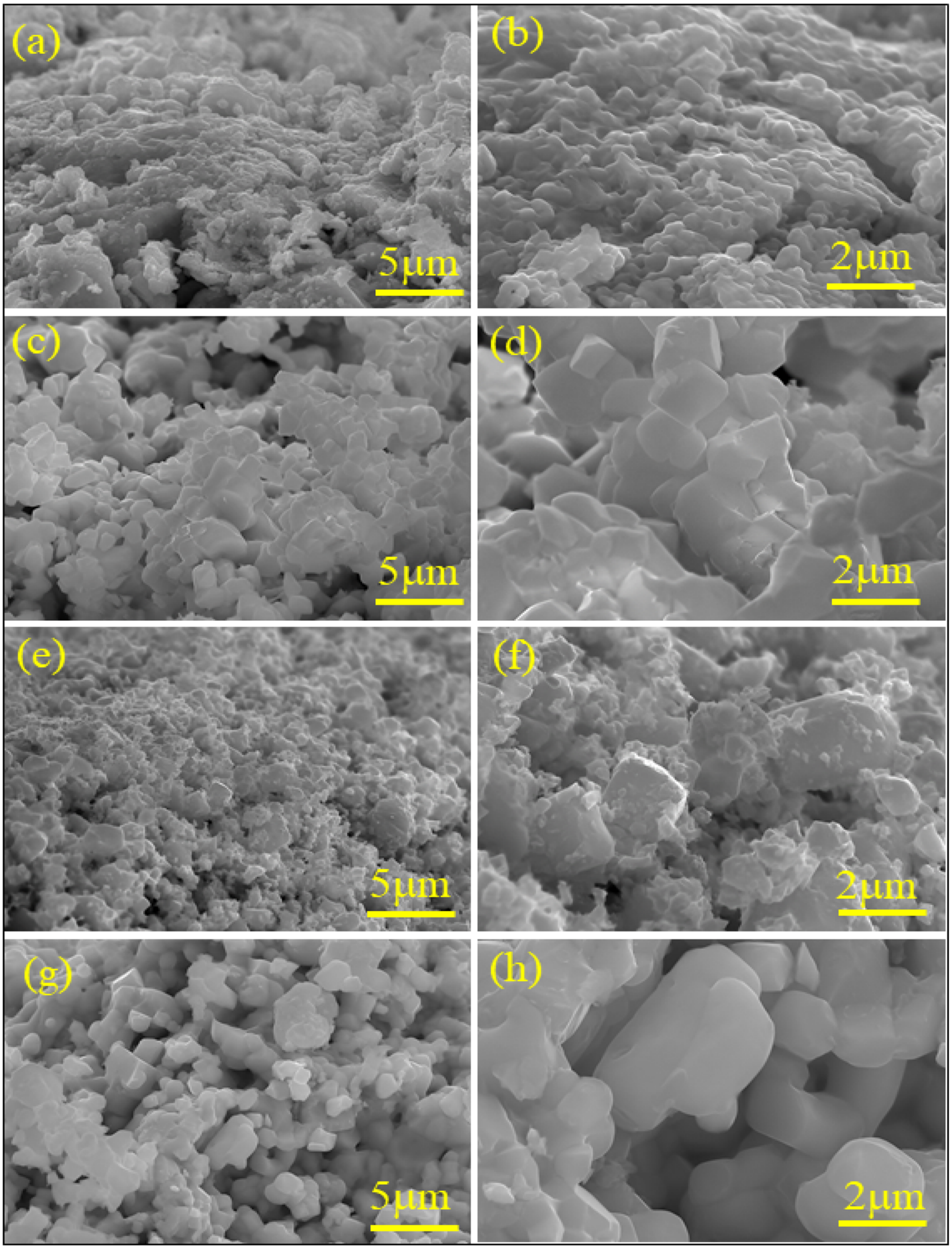

Fig. 4 FE-SEM images of fractured surfaces at two magnifications: (a and b) pristine $Co_{3.6}Ni_{0.28}Fe_{0.12}Sb_{12}$ (5 μm and 2 μm), showing densely packed aggregated particles with partially faceted surfaces and limited visible porosity; (c and d) 10 wt% PEDOT:PSS/S-AC composite (5 μm and 2 μm), where the microstructure becomes more heterogeneous with increased interparticle voids; (e and f) 20 wt% composite (5 μm and 2 μm), displaying a more developed porous network and less dense particle packing; (g and h) 40 wt% composite (5 μm and 2 μm), exhibiting large aggregated clusters accompanied by extensive void spaces and a highly porous microstructure.

The S 2p spectrum Fig. 3(f) displays characteristic S $2p_{3/2}$ and S $2p_{1/2}$ peaks within the binding-energy range of 161–164 eV, confirming the presence of sulfur species derived from the PEDOT:PSS precursor.[40,41] This binding-energy range is consistent with sulfur in thiophene-derived or carbon–sulfur bonding environments, suggesting that sulfur is incorporated within the carbonaceous phase rather than forming a separate crystalline sulfide phase.

The high-resolution C 1s XPS spectrum Fig. 3(g) exhibits a dominant peak centered at ~284.8 eV, corresponding to overlapping contributions from sp^2-hybridized C=C bonds (graphitic domains) and sp^3-hybridized C–C bonds. The broad peak profile and absence of clear peak separation indicate a structurally disordered carbon framework with mixed sp^2/sp^3 hybridization,[42] characteristic of polymer-derived amorphous carbon. Additional components located at approximately 285.5 and 288.9 eV are assigned to C–O and O–C═O functional groups, respectively, which originate from surface oxidation and defect sites within the carbon matrix. The coexistence of graphitic-like sp^2 domains and oxygen-containing functional groups suggests a heterogeneous carbon structure with localized electronic states and interfacial bonding capability.

Finally, the survey spectrum Fig. 3(h) confirms the presence of all constituent elements, including Fe, Co, Ni, In, Sb, S, C, and O. Taken together, the coexistence of sulfur species and disordered sp^2-rich carbon domains provides spectroscopic evidence for the formation of a sulfur-containing amorphous carbon interphase (S-AC) derived from PEDOT:PSS decomposition, this interphase is expected to reside preferentially at grain boundaries and is likely to contribute to the interfacial transport behavior discussed in subsequent sections.

3.3 Porosity, grain boundary, and defect-induced microstructural modifications revealed by FE-SEM and HR-TEM

The fractured surface morphologies of pristine $Co_{3.6}Ni_{0.28}Fe_{0.12}Sb_{12}$ and $In_{0.032}$ $Co_{3.6}Ni_{0.28}Fe_{0.12}Sb_{12}/x$ wt% PEDOT:PSS/S-AC composites (x = 10, 20, and 40) were examined by field-emission scanning electron microscopy (FE-SEM), with representative images shown in Fig. 4(a–h). The pristine skutterudite sample Fig. 4(a) and (b) consists of densely packed aggregated particles with partially faceted surfaces and relatively limited visible porosity, indicating a comparatively compact microstructure. Upon incorporation of 10 wt% PEDOT:PSS/S-AC and indium Fig. 4(c) and (d), the microstructure becomes more heterogeneous, and the density of interparticle voids increases, suggesting that polymer incorporation disrupts particle packing during composite formation.

At higher polymer loadings of 20 and 40 wt% Fig. 4(e–h), the overall morphology remains dominated by irregular aggregated particles, while the void density and porous character become increasingly pronounced. In particular, the 40 wt% composite exhibits a highly porous structure with extensive void spaces and particle aggregation, indicating substantial microstructural modification induced by the higher organic content and polymer decomposition during heat treatment.

The progressive increase in void density observed in the SEM images is consistent with the porosity values estimated from density measurements, confirming that the incorporation of PEDOT:PSS/S-AC systematically increases the porosity of the composite structure.

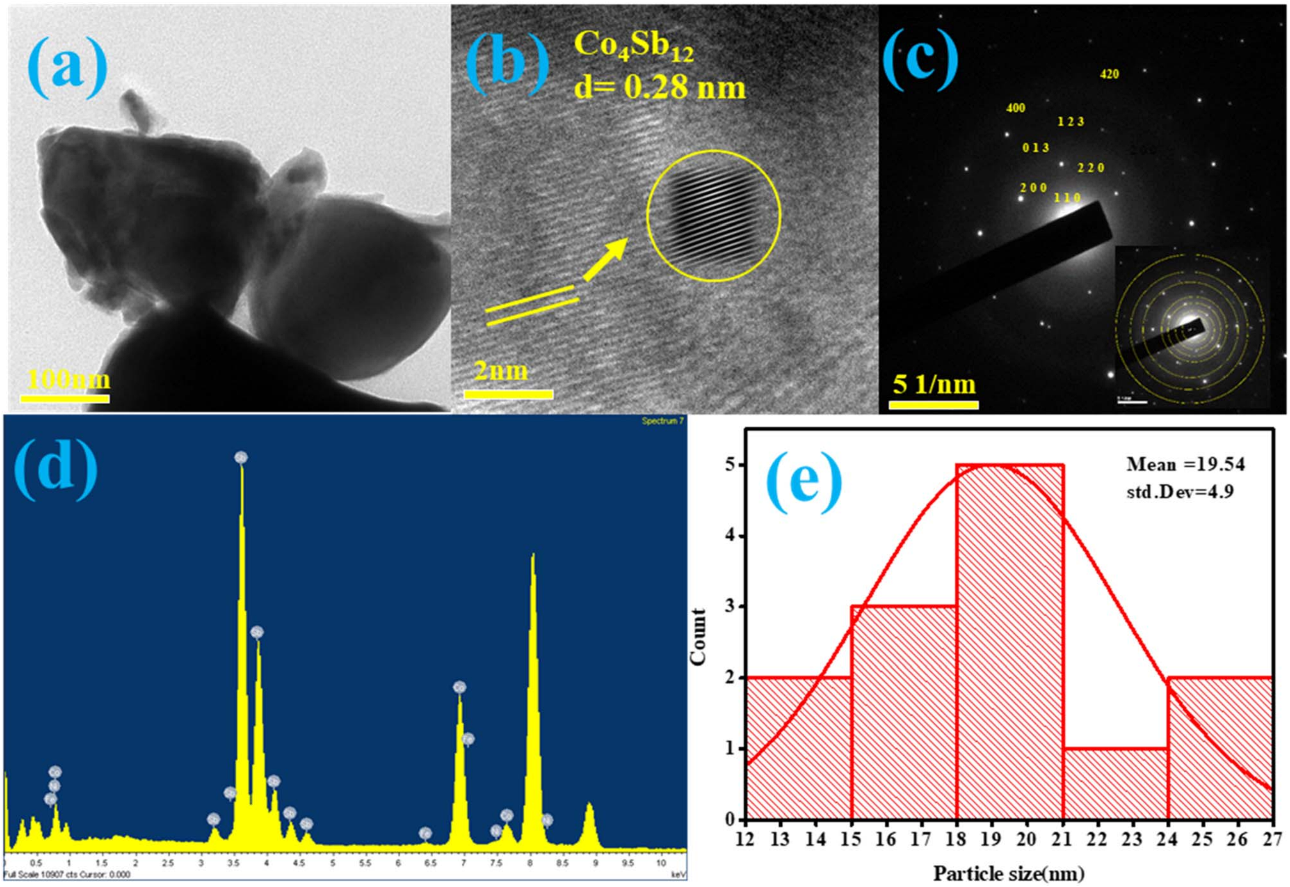

Fig. 5 (a) TEM images of particles at 100 nm scale; (b) HR-TEM image of $Co_{3.6}Ni_{0.28}Fe_{0.12}Sb_{12}$ nanocrystals showing lattice fringe patterns and d-spacing (inset); (c) selected-area electron diffraction (SAED) pattern of $Co_{3.6}Ni_{0.28}Fe_{0.12}Sb_{12}$ composites; (d) elemental mapping of $Co_{3.6}Ni_{0.28}Fe_{0.12}Sb_{12}$ composites showing uniform distribution of Co, Ni, Fe, and Sb; (e) particle size distribution histogram of $Co_{3.6}Ni_{0.28}Fe_{0.12}Sb_{12}$ composites.

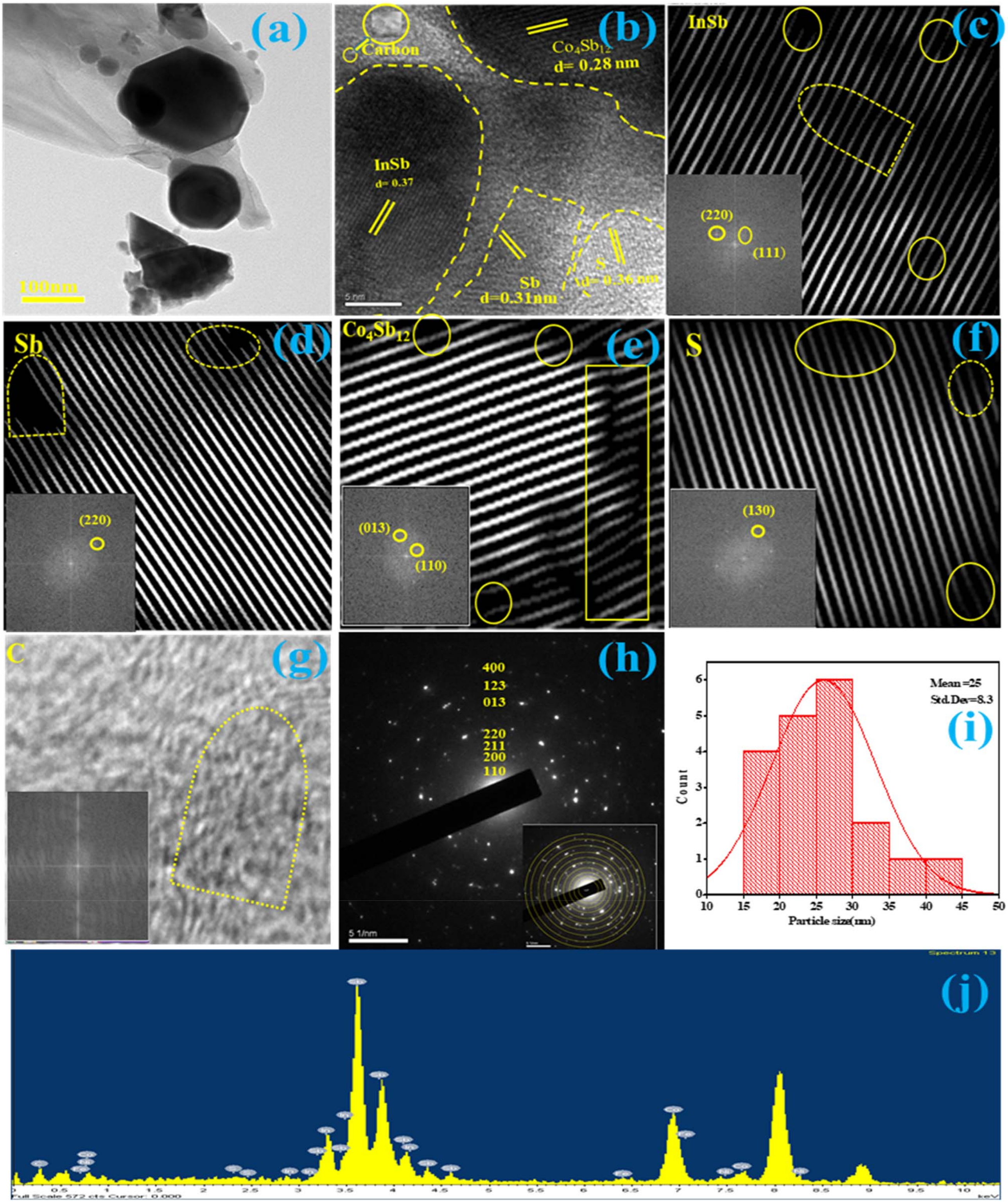

Fig. 6 (a) TEM image of $In_{0.032}Co_{3.6}Ni_{0.28}Fe_{0.12}Sb_{12}$ spherical nanoparticles at 100 nm scale; (b) HRTEM image of $In_{0.032}Co_{3.6}Ni_{0.28}Fe_{0.12}Sb_{12}$ showing nanocrystalline grains and grain boundaries; (c) FFT pattern displaying lattice spacing of the InSb phase; (d) FFT pattern of the Sb phase revealing dislocations and lattice distortion; (e) FFT pattern showing lattice spacing of the Co_4Sb_{12} structure with grain boundaries and dislocations; (f) FFT pattern of the sulfur phase displaying associated dislocations; (g) FFT pattern of the amorphous PEDOT:PSS phase; (h) SAED pattern showing distinct diffraction rings from the 40 wt% PEDOT:PSS/S-AC/$In_{0.032}Co_{3.6}Ni_{0.28}Fe_{0.12}Sb_{12}$ composite; (i) particle size distribution histogram showing average diameter of 15–44 nm; (j) elemental mapping revealing homogeneous distribution of In, Co, Ni, Fe, Sb, C, and S throughout the composite.

The average atomic percentages obtained from EDS analysis for the nominal compositions of pristine $Co_{3.6}Ni_{0.28}Fe_{0.12}Sb_{12}$ and $In_{0.032}Co_{3.6}Ni_{0.28}Fe_{0.12}Sb_{12}$/PEDOT:PSS/S-AC composites containing 10, 20, and 40 wt% HNO_3-treated PEDOT:PSS/S-AC are summarized in Table S2.

The nanostructural features of pristine $Co_{3.6}Ni_{0.28}Fe_{0.12}Sb_{12}$ and $In_{0{\cdot}032}Co_{3.6}Ni_{0.28}Fe_{0.12}Sb_{12}$ wt% PEDOT:PSS/S-AC composites were investigated by transmission electron microscopy (TEM), high-resolution TEM (HRTEM), selected-area electron diffraction (SAED), fast Fourier transform (FFT) analysis, and elemental mapping, as shown in Fig. 5 and 6.

For the pristine skutterudite shown in Fig. 5(a–e), TEM images reveal nearly spherical nanoparticles with well-defined morphology. HRTEM micrographs Fig. 5(b) display well-defined nanocrystalline grains with distinct lattice fringes corresponding to a *d*-spacing of 0.28 nm (inset). The SAED pattern Fig. 5(c) exhibits distinct diffraction rings, confirming the polycrystalline nature. Elemental analysis Fig. 5(d) verifies the uniform presence of Co, Ni, Fe, and Sb throughout the material. The particle size distribution Fig. 5(e) ranges from 19–29 nm, indicating a uniform nanocrystalline structure.

For the 40 wt% PEDOT:PSS/S-AC composite Fig. 6(a–j), TEM images reveal dispersed nanograins embedded within the skutterudite matrix. HRTEM and FFT analyses indicate the presence of several crystalline domains. InSb nanograins exhibit lattice fringes of approximately 0.37 nm corresponding to the (211) plane, with noticeable dislocations evident in the FFT pattern Fig. 6(c). Additional nanograins display diffraction features consistent with Sb phases, where lattice fringes corresponding to the (220) and (111) planes are observed together with grain-boundary distortions and low-angle boundaries Fig. 6(d). Skutterudite grains with lattice spacings of ∼0.28 nm corresponding to the (013) plane of Co_4Sb_{12} are also observed Fig. 6(e). The high density of grain boundaries and dislocations within these nanoscale domains can serve as effective phonon-scattering centers, contributing to the reduction of lattice thermal conductivity; the corresponding influence on electrical transport depends on the connectivity of conductive pathways and the presence of grain-boundary potential barriers.[43]

In addition to these phases, localized HRTEM/FFT features exhibit lattice spacings of approximately 0.32–0.38 nm that are consistent with reported spacings of orthorhombic sulfur Fig. 6(f) and S7. Considering the beam sensitivity of sulfur and the surrounding amorphous carbon matrix, this observation is interpreted cautiously as suggestive of sulfur-containing nanocrystalline domains rather than definitive phase identification. The low volume fraction of sulfur-containing species explains why no corresponding diffraction peaks are detected in XRD measurements. The sulfur is believed to originate from the decomposition of PEDOT:PSS during the heat treatment process.

The PEDOT:PSS-derived carbon phase appears predominantly amorphous Fig. 6(g), consistent with the carbonization behavior commonly reported for PEDOT:PSS-derived carbons in thermoelectric composites.[44] The selected-area electron diffraction (SAED) pattern Fig. 6(h) further confirms the polycrystalline nature of the composite structure. Particle size distribution obtained from TEM image analysis shows nanograin diameters ranging from approximately 15 to 44 nm Fig. 6(i), indicating the coexistence of multiple nanoscale phases. Elemental mapping Fig. 6(j) confirms the distribution of In, Co, Ni, Fe, Sb, C, and S throughout the composite.

Overall, TEM and elemental analyses reveal that pristine $Co_{3.6}Ni_{0.28}Fe_{0.12}Sb_{12}$ possesses a relatively uniform nanocrystalline structure, whereas incorporation of PEDOT:PSS/S-AC leads to the formation of a multiphase composite containing InSb, Sb, sulfur-containing domains, and amorphous carbon together with refined skutterudite grains. The InSb nanograins act as effective phonon scatterers, while Sb inclusions and sulfur-rich interfacial regions introduce additional grain-boundary distortions that further suppress lattice thermal conductivity. Meanwhile, the amorphous carbon interphase introduces numerous interfaces and contributes to the formation of intergranular transport pathways within the hybrid system. Collectively, these structural features create a highly heterogeneous nanostructure with abundant phonon-scattering centers, which plays a key role in reducing phonon transport and enhancing the overall thermoelectric performance.

3.4 Effects of PEDOT:PSS-sulfur-doped amorphous carbon on electronic transport in $In_{0.032}Co_{3.6}Ni_{0.28}Fe_{0.12}Sb_{12}$

3.4.1 On resistivity reduction and Hall mobility enhancement by polymer/S-AC conductive interconnects. As shown in Fig. 7(a), pristine $Co_{3.6}Ni_{0.28}Fe_{0.12}Sb_{12}$ exhibits non-metal-like transport behavior with the highest electrical resistivity (ρ), decreasing from ∼22 to ∼17 mΩ cm between 325 and 700 K. Introducing HNO_3-treated PEDOT:PSS/S-AC into the In-filled matrix ($In_{0.032}Co_{3.6}Ni_{0.28}Fe_{0.12}Sb_{12}$) does not reduce resistivity at the lowest loading: the 10 wt% composite is slightly more resistive than $In_{0.032}Co_{3.6}Ni_{0.28}Fe_{0.12}Sb_{12}$. However, beyond 10 wt% the resistivity decreases progressively with increasing polymer content, with the 40 wt% composite reaching ≈3.37 mΩ cm over the measured temperature range. This threshold-like reduction indicates that the polymer-derived interphase becomes increasingly effective once sufficient interfacial coverage is established, suggesting that the organic-inorganic hybridization progressively improves electrical connectivity across the polycrystalline network.

Hall measurements at 325 K further reveal pronounced changes in carrier transport. Pristine $Co_{3.6}Ni_{0.28}Fe_{0.12}Sb_{12}$ exhibits a carrier concentration of $n \approx 2.69 \times 10^{20}$ cm^{-3} and a Hall mobility of $\mu \approx 1.04$ cm^2 V^{-1} s^{-1}, indicating strong carrier scattering in the polycrystalline lattice. Upon addition of 10 wt% polymer, the carrier concentration decreases to 7.03×10^{19} cm^{-3} while the Hall mobility increases dramatically to 19.5 cm^2 V^{-1} s^{-1}. At higher loadings, n remains relatively stable (6.91×10^{19} and 6.62×10^{19} cm^{-3} for 20 and 40 wt%, respectively), whereas μ continues to increase to 24.9 and 29.2 cm^2 V^{-1} s^{-1}. According to the relation $\sigma = ne\mu$, the substantial mobility enhancement dominates the transport behavior, explaining the observed decrease in resistivity despite the reduction in carrier concentration. This trend is also summarized in the n–μ plot at 325 K (Fig. S8), which clearly shows that the conductivity enhancement correlates primarily with the large increase in Hall mobility rather than with carrier concentration.

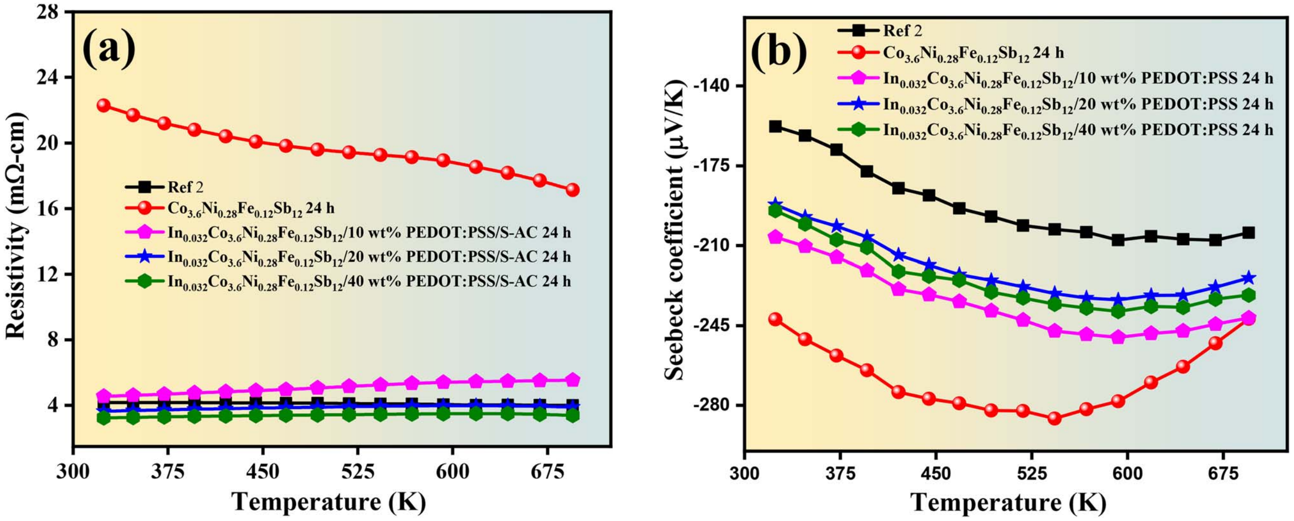

Fig. 7 Temperature dependence of electronic transport properties for pristine $Co_{3.6}Ni_{0.28}Fe_{0.12}Sb_{12}$ and $In_{0.032}Co_{3.6}Ni_{0.28}Fe_{0.12}Sb_{12}$/PEDOT:PSS/S-AC composites with 10, 20, and 40 wt% HNO_3-treated PEDOT:PSS/S-AC, sintered at 853 K for 24 h: (a) electrical resistivity, (b) Seebeck coefficient.

These trends can be interpreted using a Matthiessen-type decomposition of the polycrystalline resistivity,

$$\rho_{\text{total}} = \rho_{\text{mat}} + \rho_{\text{gb}} + \rho_{\text{int}} \tag{2}$$

where ρ_{mat} represents the intrinsic resistivity of the $Co_{3.6}Ni_{0.28}Fe_{0.12}Sb_{12}$ skutterudite lattice (phonon and impurity scattering), ρ_{gb} accounts for grain-boundary and interfacial barrier scattering, and ρ_{int} includes additional contributions arising from secondary phases or interfacial regions[9]. Indium filling primarily optimizes carrier concentration and correlates with reduced intrinsic lattice resistivity, whereas the pronounced increase in Hall mobility observed in the composites indicates that the grain-boundary contribution (ρ_{gb}) is substantially reduced upon polymer incorporation.

This behavior can be further rationalized within the framework of interface contact band theory in heterogeneous composites. In polycrystalline thermoelectric materials, grain boundaries typically introduce potential barriers that impede carrier transport and reduce carrier mobility. When a secondary phase forms at these boundaries, the band alignment between the matrix and the interfacial phase can modify the barrier height and carrier transmission probability. In the present system, the PEDOT:PSS-derived sulfur-doped amorphous carbon (S-AC) phase forms thin intergranular layers surrounding skutterudite grains, as revealed by SEM and TEM observations. Such interfacial engineering strategies have recently been demonstrated to effectively modulate carrier transport and phonon scattering in thermoelectric materials.[45,46] Raman spectroscopy further confirms the presence of disordered sp^2 carbon domains, indicated by the characteristic D and G bands associated with graphitic-like carbon structures. The relatively high I_D/I_G ratio (~2.1) indicates the presence of highly disordered sp^2 carbon regions containing localized π-electron states that can facilitate carrier tunneling across thin intergranular carbon layers. Consequently, the S-AC interphase can effectively reduce the grain-boundary barrier height and passivate interfacial defect states, thereby enhancing carrier transmission across grain boundaries and leading to the substantial mobility increase observed in the composites.

To further examine the evolution of electrical connectivity, the conductivity was fitted using a percolation-type relation, $\sigma(\phi) = \sigma_0(\phi - \phi_c)^t$ for $\phi > \phi_c$, where ϕ represents the PEDOT:PSS/S-AC volume fraction converted from weight fractions (10, 20, and 40 wt%, corresponding to $\phi \approx 0.423$, 0.595, and 0.746).[47] The fitting yields an apparent threshold $\phi_c \approx 0.255$ and exponent $t \approx 0.318$ ($R^2 \approx 0.9999$). We emphasize that this relation is used here primarily as a phenomenological descriptor of connectivity evolution rather than as evidence of classical universal percolation. Unlike conventional conductor–insulator composites, the present material system consists of an already conductive skutterudite matrix combined with a conductive polymer-derived interphase, forming a conductor–conductor hybrid system in which transport improvement arises from modification of existing grain-boundary pathways.

Microstructural observations support this interpretation. FE-SEM images (Fig. 4) show that increasing PEDOT:PSS/S-AC loading progressively modifies the fracture morphology from densely packed skutterudite grains to a more porous structure with increasingly interconnected intergranular regions. At higher polymer loadings (20–40 wt%), voids and aggregated particles become more prominent, suggesting that the polymer-derived phase preferentially occupies grain-boundary and interstitial regions. TEM analysis further reveals a multiphase nanostructure consisting of skutterudite grains together with InSb and Sb nanophases and amorphous carbon derived from PEDOT decomposition (Fig. 6). The large density of interfaces, grain boundaries, and amorphous interphases creates numerous junctions across which carriers can propagate through tunneling or hopping across thin interfacial barriers. Consequently, the strong reduction in resistivity observed between 10 and 40 wt% is consistent with tunneling-assisted transport within a segregated interfacial network rather than with a classical percolation transition.

Overall, the PEDOT:PSS-derived S-AC interphase plays a dual functional role. It reduces grain-boundary resistance and enhances carrier mobility through interfacial transport modification, while simultaneously introducing additional phonon-scattering centers that contribute to the suppression of lattice thermal conductivity. The influence of this interfacial framework on lattice thermal transport is discussed separately in Section 3.6.1 using porosity-only effective-medium-theory (EMT) baselines.

3.4.2 Polymer-derived interfaces, weighted mobility, effective mass, and power factor. As shown in Fig. 7(b), all compositions are n-type over 325–700 K. The pristine $Co_{3.6}Ni_{0.28}Fe_{0.12}Sb_{12}$ shows its $|S|$ maximum at ≈ 543 K, whereas all In-filled samples—regardless of polymer loading—show the $|S|(T)$ maximum at ≈ 592 K. Thus, the shift of $|S|_{\max}$ to higher temperature is driven by In filling; polymer loading mainly modulates the magnitude of $|S|$. Using the Goldsmid–Sharp (GS) relation on the compositions that display a clear bipolar onset, the effective gap increases from ~0.246 eV (pristine) to ~0.277–0.283 eV for the 20–40 wt% composites, indicating reduced bipolar backflow. For the 10 wt% sample, the metal-like $\rho(T)$ renders GS inapplicable; the ~0.296 eV value should be treated only as an indicative upper bound and is not used for interpretation.

The Seebeck coefficient is directly proportional to both the effective mass and temperature, while being inversely proportional to the carrier concentration, as described by the following expression,[9]

$$S = \frac{8\pi^2 k_B{}^2}{3eh^2} m^* T\left(\frac{\pi}{3n}\right)^{2/3} \tag{3}$$

where k_B is the Boltzmann constant, e the carrier's charge, h the Planck constant, m^* the carrier effective mass of the charge carrier, T the temperature, and n the charge carrier concentration. However, in our composite material, when PEDOT:PSS/S-AC is added, compared with the pristine $Co_{3.6}Ni_{0.28}Fe_{0.12}Sb_{12}$, the $|S|$ is reduced at 10 wt% and 20 wt%, but compared to 20 wt%, it is increased again at 40 wt%. This complex behavior may be caused by competing effects such as energy filtering at the interfaces, changes in carrier concentration and band structure modification.

To probe carrier pathways, we evaluate the weighted mobility μ_w from σ and S, given by[48]

$$\mu_w = \frac{3h^3}{8\pi e\rho(2m_e k_B T)^{3/2}}\left[\frac{\exp\left[\frac{|S|}{k_B/e}-2\right]}{1+\exp\left[-5\left(\frac{|S|}{k_B/e}-1\right)\right]} + \frac{\frac{3}{\pi^2}\frac{|S|}{k_B/e}}{1+\exp\left[5\left(\frac{|S|}{k_B/e}-1\right)\right]}\right] \tag{4}$$

where h, e, ρ, k_B, m_e, S, and T are Planck's constant, the carrier's charge, electrical resistivity in mΩ-cm, the Boltzmann constant, the electron's rest mass, Seebeck coefficient, and absolute temperature, respectively. As shown in Fig. 8(a), $\mu_w(T) \propto T^{-x}$ with exponents $x = 0.82$ (pristine) and $x = 1.03$, 0.93, 0.88 for 10, 20, and 40 wt% composites, respectively. The composites maintain a higher absolute μ_w than pristine over the entire range, consistent with polymer-assisted intergranular bridging that reduces boundary resistance. Within the $In_{0.032}Co_{3.6}Ni_{0.28}Fe_{0.12}Sb_{12}$/PEDOT:PSS/S-AC composite series, the mobility exponent x decreases modestly with increasing polymer loading (from ~1.03 to ~0.88). The relatively small variation of the exponent x also indicates that multiple scattering mechanisms coexist in the composite system rather than a single dominant scattering process. Such behavior suggests that, in addition to

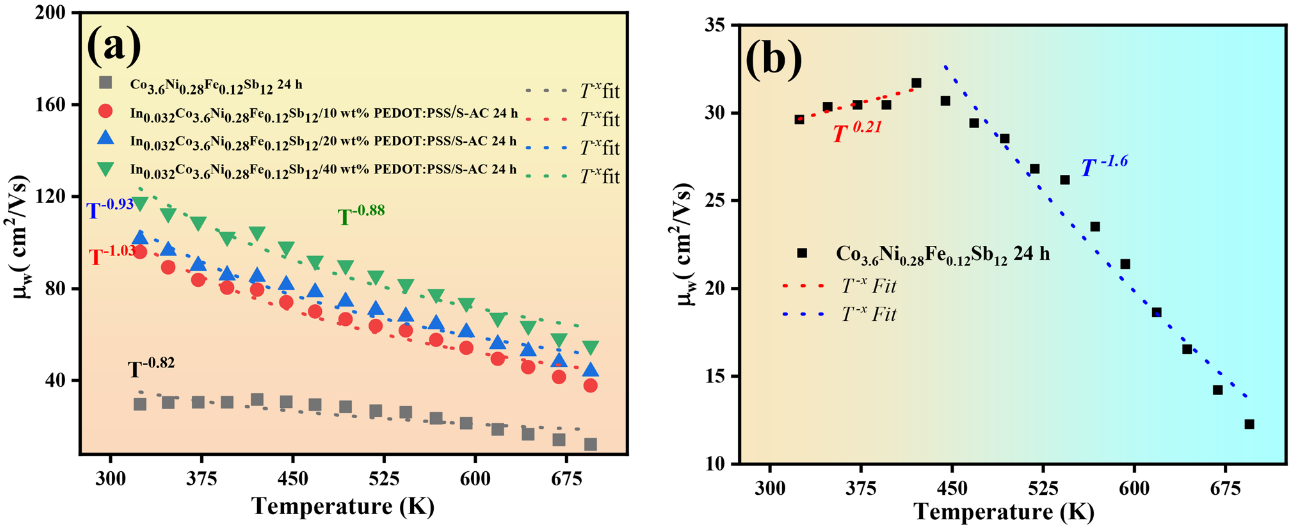

Fig. 8 Temperature-dependent weighted mobility for (a) $Co_{3.6}Ni_{0.28}Fe_{0.12}Sb_{12}$, and $In_{0.032}Co_{3.6}Ni_{0.28}Fe_{0.12}Sb_{12}$/PEDOT:PSS/S-AC composites with 10, 20, and 40 wt% HNO_3-treated PEDOT:PSS/S-AC sintering at 853 K for 24 hours, (dotted line represents temperature power laws fit) and (b) pristine $Co_{3.6}Ni_{0.28}Fe_{0.12}Sb_{12}$ (dotted line represents temperature power law fit-to clear understanding of the transport behaviour), respectively.

acoustic-phonon scattering, temperature-insensitive scattering processes associated with interfacial defects and grain boundaries increasingly contribute to carrier transport. Meanwhile, the polymer-derived S-AC interphase improves intergranular connectivity, which facilitates carrier transmission across grain boundaries and leads to the observed increase in carrier mobility and reduction in electrical resistivity ρ.

The temperature dependence of the weighted mobility μ_w further reveals a crossover between different scattering regimes. In the pristine sample, μ_w increases slightly with temperature up to $\approx$ 425 K, following approximately $\mu_w \propto T^{0.21}$(Fig. 8(b)). This weak positive temperature dependence is consistent with a regime where thermally activated carriers progressively overcome grain-boundary barriers or reduce the relative contribution of ionized-impurity scattering. At higher temperatures ($T \gtrsim$ 425 K), μ_w decreases with temperature according to $\mu_w \propto T^{-1.6}$, approaching the acoustic-phonon scattering limit. This crossover indicates that carrier transport gradually becomes phonon-limited at elevated temperatures.

Furthermore, we estimate the Seebeck effective mass m_S^* using the Snyder–Pereyra relation from measured $S(T)$ and Hall carrier concentration n_H, given by[49]

$$m_S^* = \frac{h^2}{2k_BT}\left(\frac{3n_H}{16\sqrt{\pi}}\right)^{2/3}\left[\frac{\left(\exp\left[\frac{|S|}{k_B/e}-2\right]-0.17\right)^{2/3}}{1+\exp\left[-5\left(\frac{|S|}{k_B/e}-\frac{k_B/e}{|S|}\right)\right]} + \frac{\frac{3}{\pi^2}\left(\frac{2}{\sqrt{\pi}}\right)^{2/3}\frac{|S|}{k_B/e}}{1+\exp\left[5\left(\frac{|S|}{k_B/e}-\frac{k_B/e}{|S|}\right)\right]}\right] \quad (5)$$

where m_S^* represents the Seebeck effective mass, n_H is the Hall carrier concentration of the charge, T the absolute temperature, S the Seebeck coefficient, k_B the Boltzmann constant, and e the carrier charge. The extracted m_S^* shows a consistent decreasing trend with increase of PEDOT:PSS/S-AC content, among which 10 wt%, 20 wt% and 40 wt% the effective mass of wt% samples is 8.05, 2.42, 2.11 and 2.10 m_e, respectively. The concurrent drop in m_S^* and rise in μ_w indicate that polymer-derived S-AC interphases primarily enhance the effective mobility by reducing grain-boundary resistance (longer τ), while the reduced DOS-related effective mass primarily reflects changes in the electronic density of states rather than being the dominant factor controlling mobility. Because $\mu_w \propto \mu(m^*/m_e)^{3/2}$ and m_S^* estimates the DOS mass entering μ_w, the observed rise of μ_w alongside a reduced m_S^* at 20–40 wt% is consistent with increased relaxation time τ, implying mobility gains due to polymer-derived S-AC interphase bridging (lower grain-boundary resistance).

Thus, increased μ_w alongside reduced m_S^* at 20–40 wt% reflects a mobility-dominated improvement rather than a density-of-states enhancement, highlighting that PEDOT:PSS/S-AC interphases act mainly by suppressing boundary resistance rather than altering intrinsic band curvature.

As shown in Fig. 9, the concurrent evolution of σ and S yields an increase in power factor (PF=$S^2\sigma$). All samples exhibit maxima around 550–600 K; the magnitude scales with polymer content, reaching ~16.4 μW cm^{-1} K^{-2} at 600 K (~16.0 μW cm^{-1} K^{-2} at 700 K) for the 40 wt% composite. The monotonic enhancement of PF with polymer loading is therefore a direct manifestation of higher μ_w and improved interfacial connectivity. The improvement in electronic transport does not contradict the strong suppression of κ_L observed subsequently. Both effects originate from the same polymer-derived S-AC interfacial network.

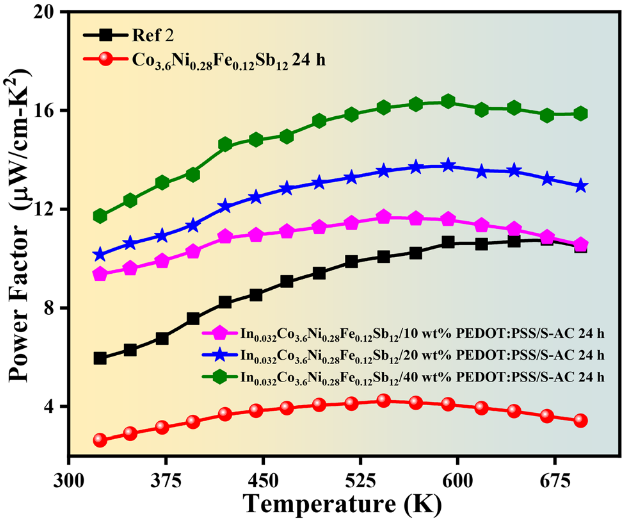

Fig. 9 Temperature dependence of power factor for pristine $Co_{3.6}Ni_{0.28}Fe_{0.12}Sb_{12}$ and $In_{0.032}Co_{3.6}Ni_{0.28}Fe_{0.12}Sb_{12}$/PEDOT:PSS/S-AC composites with 10, 20, and 40 wt% HNO_3-treated PEDOT:PSS/S-AC, sintered at 853 K for 24 h.

3.5 Role of PEDOT:PSS-derived sulfur with amorphous carbon

Because the PEDOT:PSS/S-AC phase introduces both porosity and heterogeneous interfaces, its effect on transport must be considered from both electronic and phonon-scattering perspectives. As discussed in Section 3.4, the polymer-derived S-AC interphase modifies the grain-boundary environment, improves intergranular connectivity, and enhances carrier mobility. At the same time, the same interphase network introduces amorphous layers, multiphase inclusions, and micro-/mesoporous features that act as effective phonon-scattering centers. Thus, the PEDOT:PSS-derived S-AC phase serves as a unifying interfacial component that couples electrical and thermal transport.

To further elucidate this interfacial transport mechanism, a comparative analysis was conducted among three systems: pristine $Co_{3.6}Ni_{0.28}Fe_{0.12}Sb_{12}$, $Co_{3.6}Ni_{0.28}Fe_{0.12}Sb_{12}$ with 40 wt% HNO_3-treated PEDOT:PSS/S-AC (PEDOT:PSS-only), and $In_{0.032}Co_{3.6}Ni_{0.28}Fe_{0.12}Sb_{12}$ with 40 wt% HNO_3-treated PEDOT:PSS/S-AC (In-filled + PEDOT:PSS/S-AC composite).

Fig. 10(a) shows that the pristine sample exhibits relatively high resistivity, whereas the PEDOT:PSS/S-AC-only composite shows even higher resistivity due to increased porosity and structural disorder. In contrast, the In-filled PEDOT:PSS/S-AC

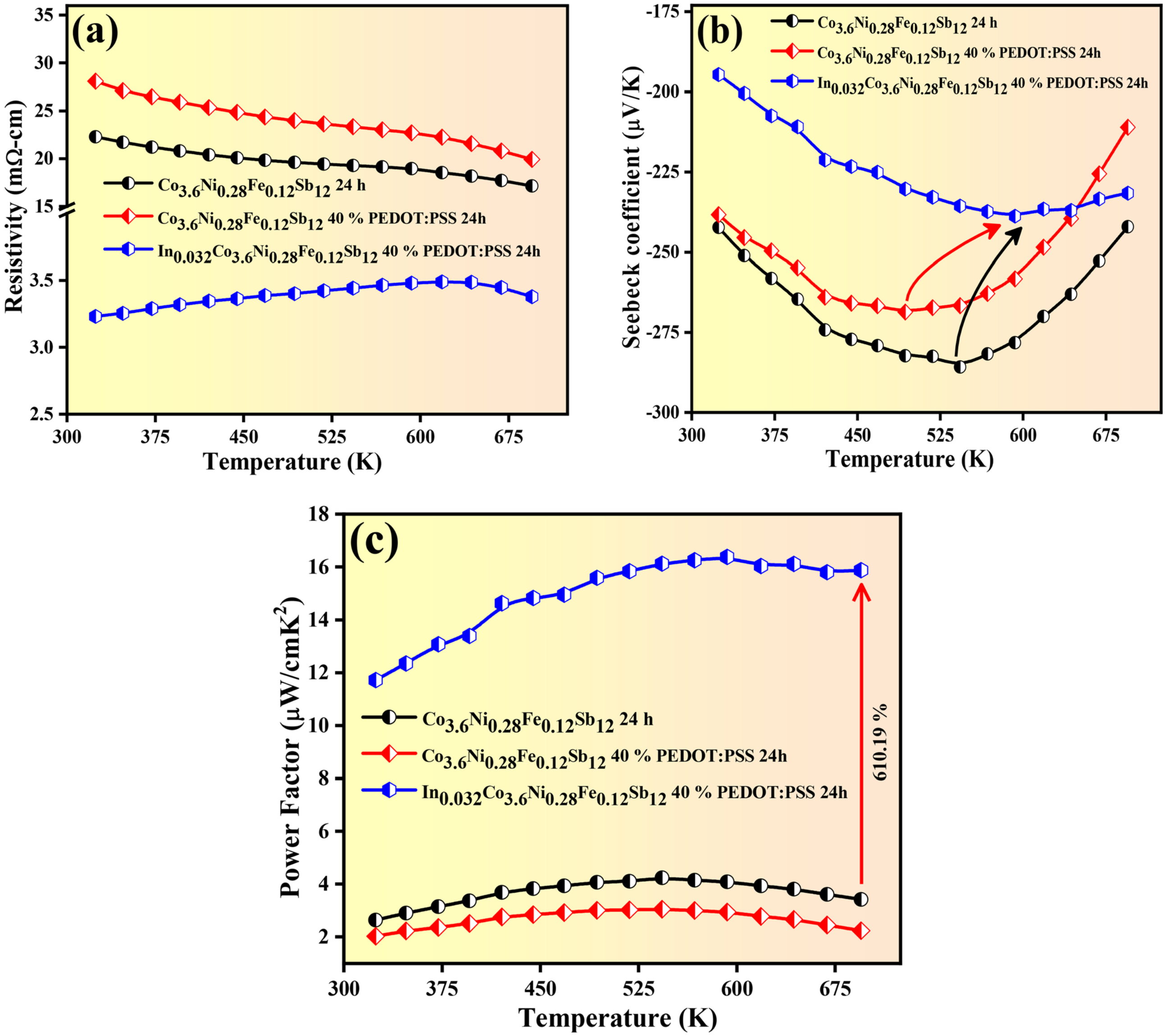

Fig. 10 Electronic transport properties of pristine $Co_{3.6}Ni_{0.28}Fe_{0.12}Sb_{12}$, $Co_{3.6}Ni_{0.28}Fe_{0.12}Sb_{12}$ with 40 wt% HNO_3-treated PEDOT:PSS/S-AC (PEDOT:PSS-only), and $In_{0.032}$ $Co_{3.6}Ni_{0.28}Fe_{0.12}Sb_1$with 40 wt% HNO_3-treated PEDOT:PSS/S-AC (In-doped composite), sintered at 853 K for 12 h: (a) electrical resistivity, (b) Seebeck coefficient, and (c) power factor.

composite exhibits a dramatic reduction in resistivity (∼3.23 mΩ cm at 325 K), corresponding to reductions of 85.5% and 88.5% compared to the PEDOT:PSS-only and pristine samples, respectively. This substantial improvement arises from a synergistic effect of indium-induced carrier concentration enhancement and interfacial conduction pathways provided by the sulfur-carbon interphase.

Fig. 10(b) confirms n-type conduction for all samples. The PEDOT:PSS/S-AC-only composite exhibits slightly larger $|S|$ values, consistent with reduced carrier concentration, whereas the In-filled composite shows lower $|S|$ values due to increased carrier concentration and Fermi-level shift. Despite this reduction, the overall thermoelectric performance is enhanced.

As shown in Fig. 10(c), the power factor (PF) is significantly improved in the In-filled PEDOT:PSS/S-AC composite, reaching ∼16.4 μW cm^{-1} K^{-2} at ∼600 K, representing a 301% and 457% enhancement over the pristine and PEDOT:PSS-only samples, respectively. These results confirm that the polymer-derived S-AC interphase enhances interfacial carrier transport, while indium filling further optimizes carrier concentration, leading to a synergistic improvement in electronic performance. These results establish that the interfacial S-AC network simultaneously governs carrier transport and sets the stage for the thermal transport behavior discussed in the following section.

3.6 Effect of polymer-derived porosity and interphases on thermal conductivity

Building on the interfacial transport mechanism established in Section 3.5, the PEDOT:PSS-derived S-AC interphase not only enhances electrical conductivity through improved intergranular carrier transport (as evidenced by the substantial reduction

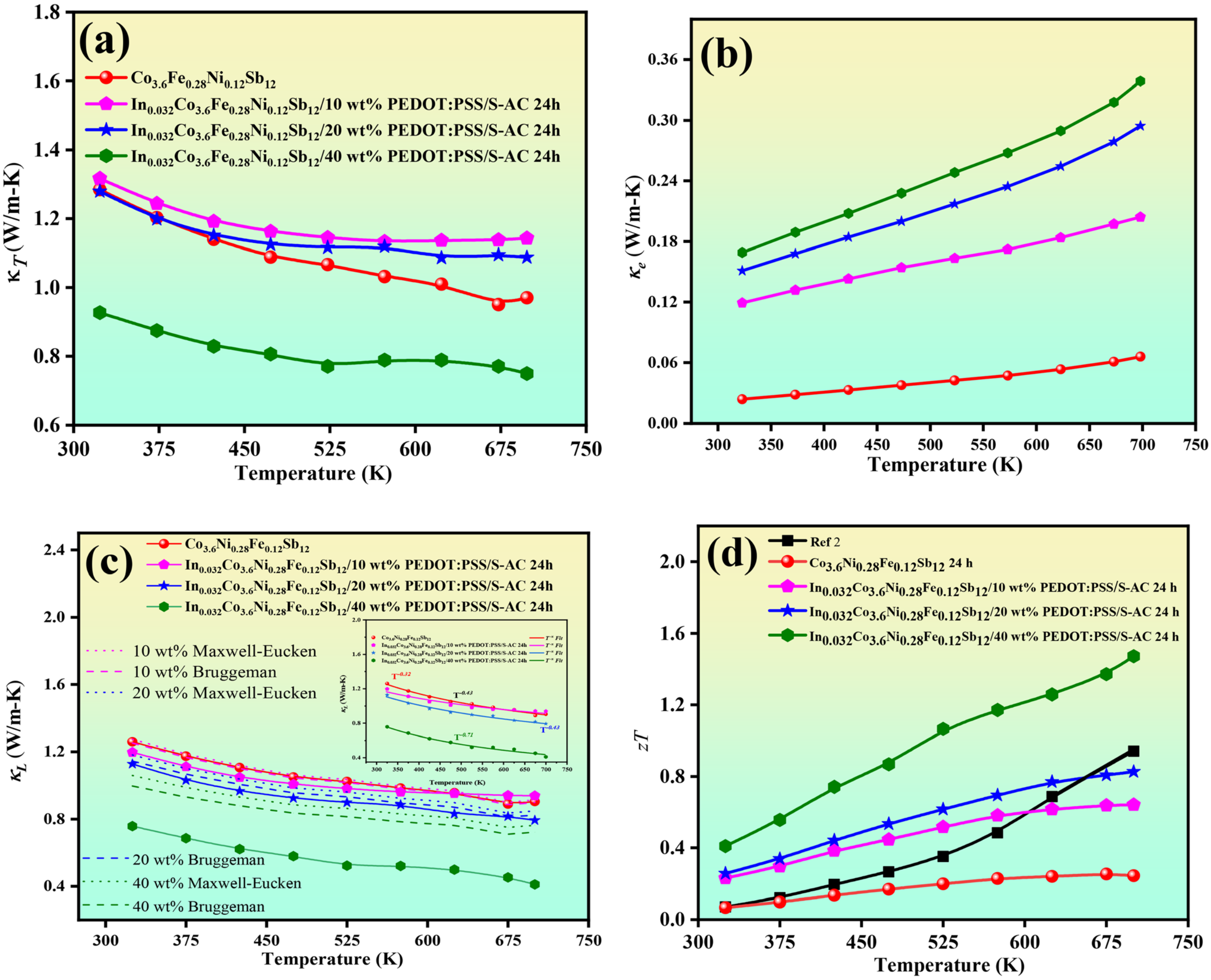

Fig. 11 (a) Temperature dependence of total thermal conductivity (κ_T) for pristine $Co_{3.6}Ni_{0.28}Fe_{0.12}Sb_{12}$ and $In_{0.032}Co_{3.6}Ni_{0.28}Fe_{0.12}Sb_{12}$ composites containing 10, 20, and 40 wt% PEDOT:PSS/S-AC. All samples show monotonic $\kappa_T(T)$ decreases, but distinct regimes emerge: 10–20 wt% exhibit κ_T comparable to or above the pristine due to enhanced electronic heat transport, whereas 40 wt% shows pronounced κ_T reduction associated with formation of a polymer-derived interphase. (b) Electronic thermal conductivity (κ_e), calculated using the Wiedemann–Franz relation with Lorenz numbers derived from a single-Kane-band model. (c) Lattice thermal conductivity (κ_L) as a function of temperature. κ_L decreases systematically with increasing polymer loading. The dashed and dotted curves represent porosity-only effective-medium theory (EMT) baselines calculated using the Maxwell–Eucken and Bruggeman models ($\kappa_p = 0.05$ W m^{-1} K^{-1}), respectively. The 40 wt% composite exhibits κ_L values that fall below these porosity-only predictions, indicating additional phonon-scattering contributions associated with the amorphous S-AC interphase and multiphase microstructure. (The inset shows the temperature-dependent lattice thermal conductivity (κ_L) of the composites with varying polymer content, exhibiting a systematic reduction with increasing polymer loading. Power-law fitting ($\kappa_L \propto T^{-x}$) yields exponents $x \approx 0.32$–0.47, indicating a clear deviation from purely Umklapp-limited phonon transport. This behavior suggests a dominant contribution from temperature-independent phonon scattering mechanisms, including static disorder arising from Ni/Fe alloying, interfacial scattering, and the presence of secondary phases) (d) temperature dependence of zT. Moderate polymer loadings yield incremental improvements, while the 40 wt% composite delivers the highest zT across the measured range due to combined κ_L suppression and favorable electronic transport.

in resistivity and enhancement in power factor in Fig. 10), but also introduces structural features that strongly influence phonon transport. In particular, the formation of amorphous interlayers, multiphase inclusions, and micro-/mesoporous structures provides additional phonon-scattering centers, thereby coupling electronic and thermal transport through the same interfacial framework.

Fig. 11(a) presents the total thermal conductivity (κ_T) of pristine $Co_{3.6}Ni_{0.28}Fe_{0.12}Sb_{12}$ and $In_{0.032}Co_{3.6}Ni_{0.28}Fe_{0.12}Sb_{12}$ composites containing 10, 20, and 40 wt% PEDOT:PSS/S-AC. All samples exhibit the expected decrease in κ_T with increasing temperature, reflecting enhanced phonon–phonon (Umklapp) scattering and reduced phonon mean free paths at elevated temperatures.[8,50] However, κ_T does not vary monotonically with polymer content. At 10–20 wt%, κ_T remains comparable to or slightly above that of the pristine material across large portions of the temperature range, whereas the 40 wt% composite exhibits a pronounced κ_T reduction, suggesting a transition in the dominant heat-transport mechanism at high interphase loading.

To elucidate this behavior, the electronic contribution κ_e was separated from κ_T using the Wiedemann–Franz relation, with Lorenz numbers calculated from the Kane-band model *via* the SKBcal algorithm under dominant acoustic phonon scattering.[51] As shown in Fig. 11(b), κ_e is lowest in the pristine sample, consistent with its high electrical resistivity. Incorporation of 10–20 wt% PEDOT:PSS/S-AC increases κ_e, reflecting enhanced carrier mobility and reduced grain-boundary resistance arising from interfacial bridging. This trend is consistent with the electronic transport behavior shown in Fig. 10, where improved interfacial connectivity leads to enhanced carrier transport. At these intermediate loadings, the increase in κ_e partially offsets moderate reductions in lattice thermal conductivity (κ_L), resulting in κ_T values comparable to or slightly higher than those of the pristine material.

At higher polymer loading (40 wt%), κ_e continues to follow the overall electrical conductivity trend and remains higher than that of the pristine sample. However, the polymer-derived interphase—comprising amorphous sulfur-rich carbon layers, micro-/mesoporous features, and multiphase inclusions—forms a dense heterogeneous network that strongly enhances phonon scattering. In this regime, the lattice thermal conductivity decreases substantially due to increased interface density, structural disorder, and the presence of amorphous interphases. Consequently, the pronounced suppression of κ_L dominates the overall thermal transport, leading to the lowest κ_T among all compositions.

Overall, the evolution of κ_T across the series reflects the competition between electronic and lattice heat transport. At moderate polymer loadings (10–20 wt%), improved intergranular connectivity enhances κ_e and partially compensates for κ_L suppression. At higher loading (40 wt%), however, the strong reduction in κ_L becomes the dominant factor governing thermal transport, producing the largest decrease in κ_T and consequently the highest thermoelectric performance, as reflected in the zT values shown in Fig. 11(d).

3.6.1 Lattice thermal conductivity: beyond porosity – interfacial and multiphase scattering.

Building on the interfacial framework established in Sections 3.4–3.5, the lattice thermal conductivity (κ_L) provides further insight into how the PEDOT:PSS-derived S-AC interphase influences phonon transport.

Fig. 11(c) shows the temperature dependence of κ_L for all compositions. κ_L decreases with increasing temperature, consistent with phonon–phonon (Umklapp) scattering. At 325 K, κ_L decreases from 1.26 W m^{-1} K^{-1} for the pristine sample to 1.22, 1.15, and 0.84 W m^{-1} K^{-1} for the 10, 20, and 40 wt% composites, respectively. The 40 wt% composite maintains the lowest κ_L across the entire temperature range and reaches approximately 0.55 W m^{-1} K^{-1} at 700 K. Power-law fitting ($\kappa_L \propto T^{-x}$) yields exponents $x \approx 0.32$–0.47, weaker than the canonical ∼0.5 expected for purely Umklapp-limited transport, indicating the presence of additional temperature-insensitive scattering mechanisms arising from static alloy disorder (Ni/Fe substitution), interfaces, and multiphase inclusions.[34,52]

3.6.1.1 Porosity-only EMT baselines (Maxwell–Eucken and Bruggeman). To determine whether the observed suppression of κ_L can be attributed solely to porosity dilution, porosity-only effective-medium theory (EMT) baselines were established using the Maxwell–Eucken model and the Bruggeman self-consistent approximation.[53,54] In these expressions, κ_s denotes the lattice thermal conductivity of the continuous solid matrix and κ_p the thermal conductivity of the pore phase, with ϕ representing the pore volume fraction. Maxwell–Eucken relation is given by

$$\kappa_L^{ME} = \kappa_s \frac{\kappa_p + 2\kappa_s - 2\phi(\kappa_s - \kappa_p)}{\kappa_p + 2\kappa_s + \phi(\kappa_s - \kappa_p)} \tag{6}$$

while Bruggeman self-consistent relation is given by

$$(1-\phi)\frac{\kappa_s - \kappa_{eff}}{\kappa_s + 2\kappa_{eff}} + \phi\frac{\kappa_p - \kappa_{eff}}{\kappa_p + 2\kappa_{eff}} = 0 \tag{7}$$

Because the pores are predominantly air-filled, $\kappa_p \approx 0$ W m^{-1} K^{-1} is adopted as the primary baseline, with $\kappa_p = 0.05$ W m^{-1} K^{-1} evaluated as a sensitivity case. To avoid double counting porosity in the pristine sample, $\kappa_s(T)$ was back-calculated by enforcing EMT consistency at the measured pristine porosity and subsequently applied to the composites at their respective porosities.

Under this unified porosity-only baseline, the 40 wt% composite exhibits κ_L values at both 325 K and 700 K that are 16–22% lower than Maxwell–Eucken and Bruggeman predictions as shown in Fig. 11(c), exceeding the experimental uncertainty (±5%). This deviation indicates that additional interface- and multiphase-mediated phonon-scattering mechanisms contribute beyond simple volumetric porosity dilution. These results further support that the deviation from porosity-only predictions originates from interface-dominated phonon scattering rather than simple volumetric dilution.

3.6.1.2 Interface- and multiphase-induced phonon scattering. The enhanced suppression of κ_L can be attributed to multiple cooperative phonon-scattering mechanisms introduced by the polymer-derived S-AC interphase and the associated multiphase microstructure. First, the formation of micro-/mesopores and amorphous interlayers promotes diffuse boundary (Casimir/Knudsen) scattering when structural dimensions approach dominant phonon mean free paths, thereby reducing phonon specularity and enhancing back-scattering.[55–57] Second, the sulfur-doped amorphous carbon interlayers introduce significant vibrational mismatch relative to the crystalline skutterudite matrix, generating interfacial thermal resistance and increasing the probability of phonon mode conversion and reflection.[55] Third, the presence of secondary nanophases such as InSb and Sb introduces mass contrast and local strain-field fluctuations, further shortening phonon lifetimes[58,59] and weakening the intrinsic temperature dependence of κ_L.

High-resolution TEM images Fig. 6(b–f) reveal the coexistence of crystalline InSb nanophases and surrounding amorphous carbon layers derived from PEDOT:PSS decomposition. The corresponding FFT and SAED patterns Fig. 6(d–h) confirm the crystalline nature of the InSb and Co_4Sb_{12} phases and the amorphous character of the carbon interlayer.

To provide semi-quantitative insight into the relative importance of the proposed scattering mechanisms, additional

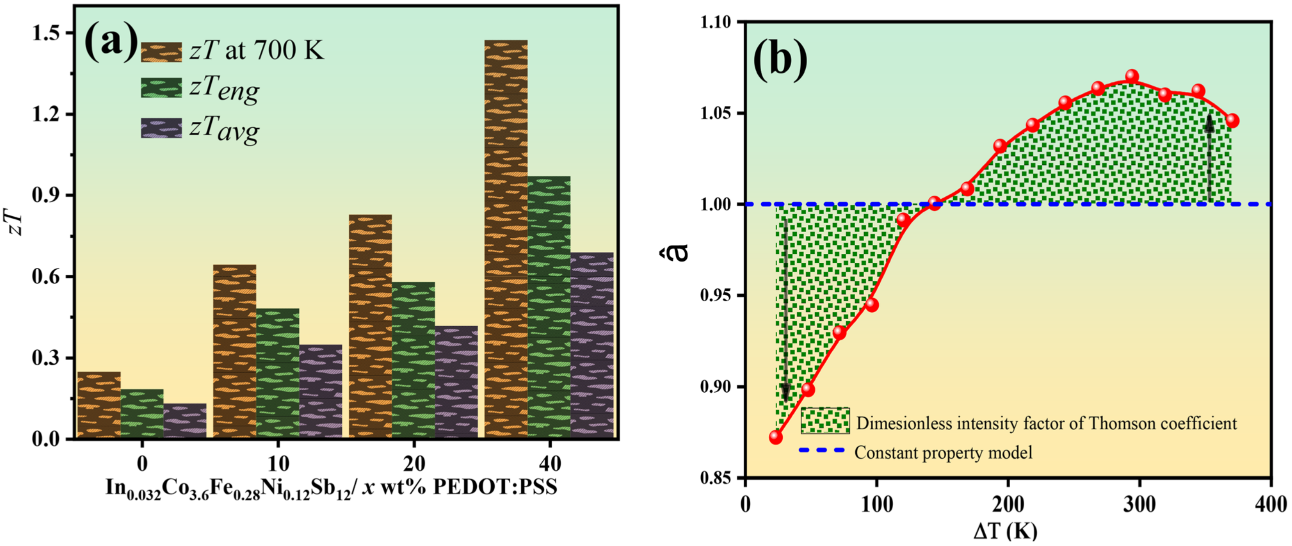

Fig. 12 (a) zT, zT_{avg}, zT_{eng}, of $Co_{3.6}Ni_{0.28}Fe_{0.12}Sb_{12}$, and 10, 20, and 40 wt% of PEDOT:PSS/S-AC $In_{0.032}Co_{3.6}Ni_{0.28}Fe_{0.12}Sb_{12}$; (b) dimensionless Thomson strength factor ($\hat{a}$) as a function of the applied temperature difference (ΔT) for $In_{0.032}Co_{3.6}Ni_{0.28}Fe_{0.12}Sb_{12}$/40 wt% PEDOT:PSS composite; the dotted curve denotes the constant-property model.

TEM analysis was performed to estimate the characteristic structural length scales in the composite. As shown in the supplementary TEM analysis (Fig. S6), ImageJ measurements performed over multiple regions yield an average interphase thickness of approximately 2.26 nm from Fig. S6(g). Statistical analysis of these features Fig. S6(i) indicates a characteristic pore diameter of approximately 16.35 nm. These two characteristic structural dimensions therefore represent distinct phonon-scattering length scales in the composite system.

Within the framework of boundary (Casimir-type) scattering, the phonon relaxation time is commonly approximated as $\tau^{-1} \propto \nu/L$, where L represents the characteristic structural length scale and ν the phonon group velocity. Consequently, smaller structural dimensions generally lead to stronger boundary scattering. Because the dominant phonon mean free path in skutterudite materials typically lies in the range of ∼10–100 nm, both the amorphous interphase thickness (∼2–3 nm) and the pore diameter (∼16 nm) fall within the effective phonon-scattering regime. The ultrathin amorphous interphase is expected to scatter short-wavelength phonons, whereas pores with dimensions on the order of ∼16 nm mainly scatter mid-wavelength phonons.

The coexistence of these two structural length scales therefore enables multi-scale phonon scattering, in which hierarchical interfaces scatter phonons across a broad spectrum of wavelengths. Consequently, the amorphous S-AC interphase is expected to make a major contribution to the suppression of lattice thermal conductivity, while pore scattering provides an additional contribution by disrupting phonon transport at larger length scales. These TEM-derived structural parameters therefore provide semi-quantitative support for the multi-scale phonon-scattering mechanism responsible for the strong κ_L suppression observed in the PEDOT:PSS-derived S-AC/skutterudite composite system.

3.7 Comprehensive assessment of thermoelectric efficiency *via zT*, average and engineering *zT*, and dimensionless strength factor

Fig. 11(d) shows the temperature dependence of zT for pristine $Co_{3.6}Ni_{0.28}Fe_{0.12}Sb_{12}$ and $In_{0.032}Co_{3.6}Ni_{0.28}Fe_{0.12}Sb_{12}$ composites containing 10, 20, and 40 wt% HNO_3-treated PEDOT:PSS/S-AC. The pristine sample exhibits the lowest zT (0.24 at 700 K), reflecting its modest power factor and relatively high lattice thermal conductivity (κ_L). With In filling and polymer-derived hybridization (amorphous carbon/sulfur residues from PEDOT:PSS), zT improves across the entire temperature range owing to enhanced electrical transport and suppressed κ_L. At 700 K, relative to the pristine sample ($zT = 0.24$), the composites reach $zT \approx 0.64$ (≈2.67×, +167%), 0.82 (≈3.42×, +242%), and 1.47 (≈6.13×, +513%) for 10, 20, and 40 wt%, respectively. These gains arise from a synergistic combination of scattering processes: Fe/Ni alloy scattering provides a strong baseline reduction in phonon transport; porosity disrupts continuous heat-conduction pathways; and amorphous carbon-rich interfacial layers derived from PEDOT:PSS act as effective phonon barriers while supplying localized electronic bridges that preserve mobility. The net effect is a substantial κ_L reduction without undue degradation of carrier transport.

Fig. 12(a) compares zT, the average dimensionless figure of merit (zT_{avg}), and the engineering dimensionless figure of merit (zT_{eng}) for the same set. The commonly used zT_{avg} provides an integrated efficiency over a temperature span and is defined as[60,61]

$$zT_{avg} = \frac{1}{T_H - T_C}\int_{T_C}^{T_H} zT\,dT \tag{8}$$

where T_H and T_C are the hot and cold side temperature, respectively. The 40 wt% composite exhibits the highest zT_{avg}, ∼0.97, which is about 5.37 times that of the pristine sample, confirming the robustness of the hybrid strategy over the operating window. While zT_{avg} offers a useful indication of material efficiency, it does not fully capture the temperature dependence of transport properties in real devices operating across large temperature gradients. For this purpose, the engineering dimensionless figure of merit (zT_{eng}) given in eqn (9) provides a more rigorous assessment. It is defined as[62]

$$zT_{\mathrm{eng}} = \frac{\left(\int_{T_{\mathrm{C}}}^{T_{\mathrm{H}}} S\ (T)\mathrm{d}T\right)^2}{\left(\int_{T_{\mathrm{C}}}^{T_{\mathrm{H}}} \rho\ (T)\mathrm{d}T\right)\left(\int_{T_{\mathrm{C}}}^{T_{\mathrm{H}}} \kappa\ (T)\mathrm{d}T\right)}\Delta T, \tag{9}$$

where $S(T)$, $\rho(T)$, and $\kappa(T)$ are the Seebeck coefficient, electrical resistivity, and thermal conductivity, respectively, and $\Delta T = T_{\mathrm{H}} - T_{\mathrm{C}}$. As shown in Fig. 12(a), the 40 wt% composite achieves $zT_{\mathrm{eng}} \approx 0.69$, about 5.39× the pristine value, highlighting its superior device-relevant performance under large temperature gradients.

The maximum conversion efficiency of thermoelectric materials also depends on the Thomson effect, which is quantified *via* the dimensionless strength factor $\hat{a}$ as shown in Fig. 12(b). By definition $\hat{a} = 1$ corresponds to a temperature-independent Seebeck coefficient. For n-type materials, $\hat{a} > 1$ implies that S becomes more negative with temperature ($\mathrm{d}S\ \mathrm{d}T^{-1} < 0$), increasing the beneficial Thomson contribution to energy conversion. We evaluate $\hat{a}$ using[62]

$$\hat{a} = \frac{S(T_{\mathrm{h}})\Delta T}{\int_{T_{\mathrm{c}}}^{T_{\mathrm{h}}} S\ (T)\mathrm{d}T} \tag{10}$$

where $S(T_{\mathrm{h}})$ is the Seebeck coefficient at T_{h}. As shown in Fig. 12(b), $\hat{a}$ varies with the applied temperature difference. For the $\mathrm{In_{0.032}Co_{3.6}Ni_{0.28}Fe_{0.12}Sb_{12}}$/40 wt% PEDOT:PSS composite, $\hat{a}$ rises with ΔT: it is below unity for small gradients ($\Delta T < 100$ K), approaches unity near $\Delta T \approx 150$ K, and exceeds 1.0 at larger ΔT, reaching a maximum of ∼1.06 around ∼300 K, before slightly declining. The dotted line in Fig. 12(b) indicates the constant-property model for reference. This behavior shows that under substantial temperature gradients the Thomson effect makes a non-negligible, favorable contribution, complementing the gains implied by zT, zT_{avg}, and zT_{eng}.

3.8 Effect of PEDOT:PSS-derived sulphur-amorphous carbon composites on phonon scattering and lattice thermal transport: Raman spectroscopic insights

To identify the mechanisms responsible for the reduction of lattice thermal conductivity in $\mathrm{Co_{3.6}Ni_{0.28}Fe_{0.12}Sb_{12}}$ and $\mathrm{In_{0.032}Co_{3.6}Ni_{0.28}Fe_{0.12}Sb_{12}}/x$ wt% $\mathrm{HNO_3}$-treated PEDOT:PSS/S-AC composites ($x = 10$, 20, 40 wt%), we examined phonon vibrations using Raman spectroscopy.

The skutterudite $\mathrm{CoSb_3}$ crystallizes in the $Im\bar{3}$ (No. 204) space group with 16 atoms per primitive cell, yielding 48 phonon modes (3 acoustic + 45 optical). Factor-group analysis gives the optical mode decomposition $2\mathrm{A_g} + 2\mathrm{E_g} + 4\mathrm{T_g}$, $2\mathrm{A_u} + 2\mathrm{E_u} + 7\mathrm{T_u}$; $\mathrm{A_g}$, $\mathrm{E_g}$, and $\mathrm{T_g}$ are Raman-active (eight symmetry-distinct modes), while $\mathrm{T_u}$ are infrared-active.[63] In filled skutterudites ($\mathrm{RCo_4Sb_{12}}$), the filler at the 2a site introduces additional low-frequency $\mathrm{T_u}$ ("rattler") modes. Fig. 13(a) shows the Raman spectra of the pristine and composite samples. The pristine compound exhibits bands at 82.1, 105.4, 131.8, 147.4, 175.4, and 182.4 $\mathrm{cm^{-1}}$. With increasing PEDOT:PSS/S-AC content, these modes systematically red-shift and broaden, indicating reduced vibrational energies and enhanced phonon scattering arising from lattice disorder, mass/strain fluctuations, and polymer-derived interfaces. All peaks were fitted with Voigt (Lorentzian–Gaussian) profiles; fitted positions and FWHM values are compiled in Table S3 for quantitative comparison.

To disentangle polymer contributions, we measured PEDOT:PSS before and after annealing at 580 °C. Pristine PEDOT:PSS shows features at 1094, 1228, 1253, 1329, 1362, 1416, and 1475 $\mathrm{cm^{-1}}$, attributable to $\mathrm{SO_3^-}$ stretching (1094 $\mathrm{cm^{-1}}$), C–C inter-ring/α–α′ thiophene stretching (1228–1253 $\mathrm{cm^{-1}}$), backbone C–C vibrations (1329–1362 $\mathrm{cm^{-1}}$), and symmetric/asymmetric C=C stretching (1416, 1475 $\mathrm{cm^{-1}}$). The 1416 $\mathrm{cm^{-1}}$ band tracks the PEDOT oxidation state (polaron/bipolaron marker).[64] After annealing, sharp polymer bands collapse into broad features at ∼1152, ∼1339, and ∼1555 $\mathrm{cm^{-1}}$. The ∼1152 $\mathrm{cm^{-1}}$ signal indicates residual sulfonate groups (incomplete PSS removal);[65] the ∼1339 $\mathrm{cm^{-1}}$ band reflects disordered $\mathrm{sp^2}$ C–C stretching (D band); and the ∼1555 $\mathrm{cm^{-1}}$ band corresponds to a down-shifted G-like mode of short-range $\mathrm{sp^2}$ domains. The intensity ratio $I_{\mathrm{D}}/I_{\mathrm{G}} \approx 2.1$ confirms formation of highly disordered amorphous/nanocrystalline carbon, consistent with TEM observations; the G-band downshift relative to crystalline graphite (∼1580 $\mathrm{cm^{-1}}$) further evidences reduced crystallite size and increased disorder.

Linewidth analysis provides a dynamical view of phonon transport. Phonon lifetimes (τ) are estimated from the Raman full width at half maximum (FWHM, Γ) using[66]

$$\tau = \frac{1}{2\pi c\Gamma} \tag{11}$$

where c is the speed of light in vacuum and Γ is the FWHM in wavenumber units ($\mathrm{cm^{-1}}$). As summarized in Table S3 and Fig. 13(e), τ decreases with increasing PEDOT:PSS/S-AC content. Shorter lifetimes signify stronger phonon scattering, correlating with the observed suppression of the lattice thermal conductivity κ_{L} (Section 3.6.1). The combined evidence—peak red-shift, linewidth broadening, and τ reduction—indicates a multi-scale scattering landscape dominated by: (i) amorphous carbon/sulfur intergranular layers that impose high interfacial thermal resistance, (ii) porosity and pore-interface coupling (diffuse boundary scattering), (iii) alloy-disorder scattering from Ni/Fe substitution, and (iv) secondary nanophases (InSb, Sb, S) that introduce mass and strain contrast.

Taken together, the Raman spectroscopic analysis, lifetime evaluation, and quantitative fits (Table S3) demonstrate that PEDOT:PSS/S-AC fundamentally modifies lattice vibrational dynamics in $\mathrm{CoSb_3}$-based skutterudites. The polymer-derived amorphous network and associated interfaces provide efficient phonon-scattering centers that drive κ_{L} below porosity-only expectations, thereby rationalizing the substantial reductions in κ_{L} and the concurrent rise in zT for high-loading composites.

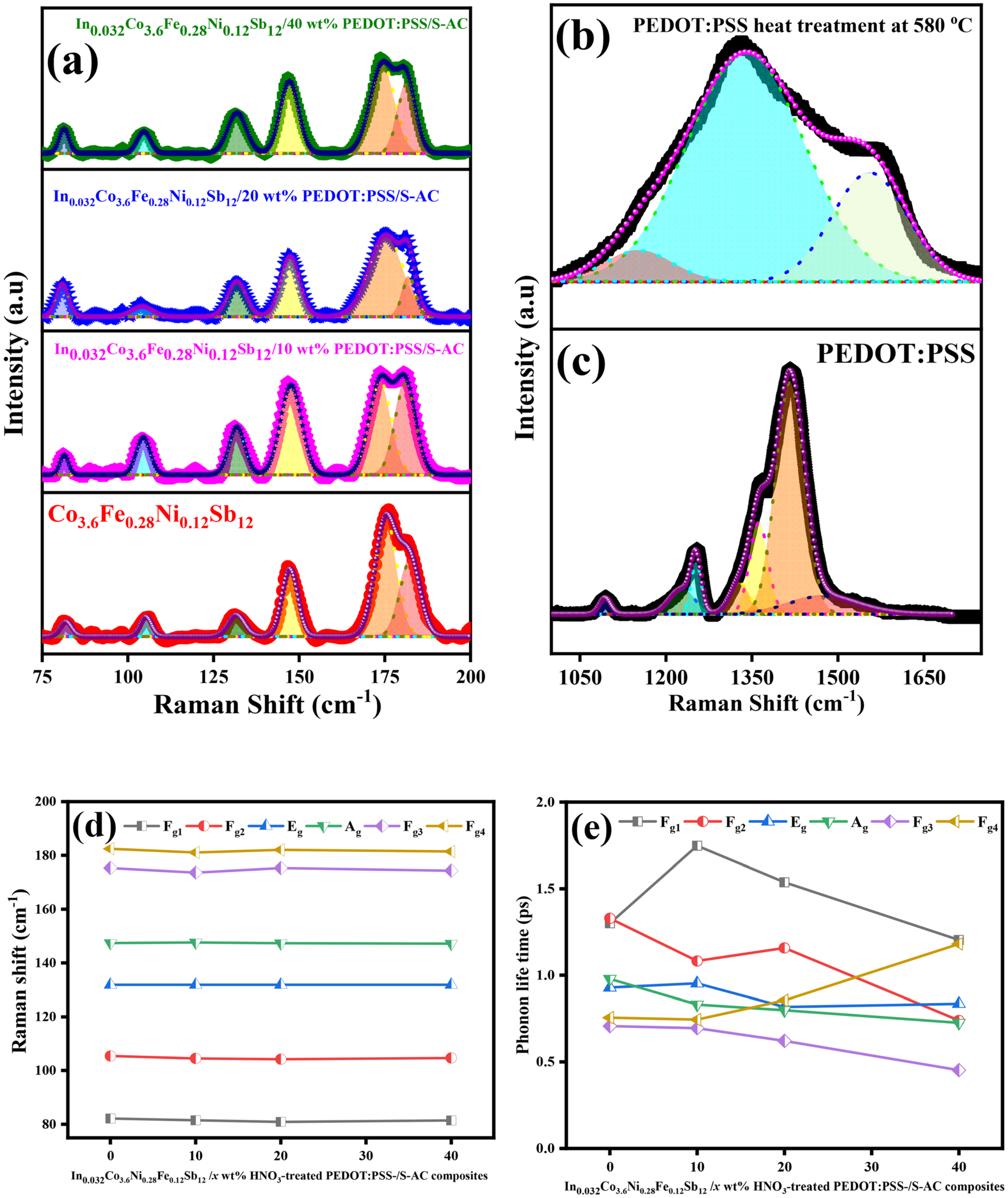

Fig. 13 Raman spectroscopy analysis of $Co_{3.6}Ni_{0.28}Fe_{0.12}Sb_{12}$ and $In_{0.032}Co_{3.6}Ni_{0.28}Fe_{0.12}Sb_{12}/x$ wt% PEDOT:PSS/S-AC composites. (a) Raman spectra at different PEDOT:PSS/S-AC contents (10, 20, 40 wt%). (b and c) Raman spectra of pristine PEDOT:PSS and $In_{0.032}Co_{3.6}Ni_{0.28}Fe_{0.12}Sb_{12}$/40 wt% PEDOT:PSS composites after thermal treatment at 580 °C. (d) Raman peak positions of pristine $Co_{3.6}Ni_{0.28}Fe_{0.12}Sb_{12}$ and $In_{0.032}Co_{3.6}Ni_{0.28}Fe_{0.12}Sb_{12}/x$ wt% HNO_3-treated PEDOT:PSS-SC composites ($x = 10, 20, 40$ wt%). A systematic red shift of the vibrational modes is observed with increasing PEDOT:PSS content, indicative of softening of phonon modes due to enhanced carrier-phonon coupling and interfacial strain effects. (e) Phonon lifetimes extracted from the full width at half maximum (FWHM) of Raman-active vibrational modes.

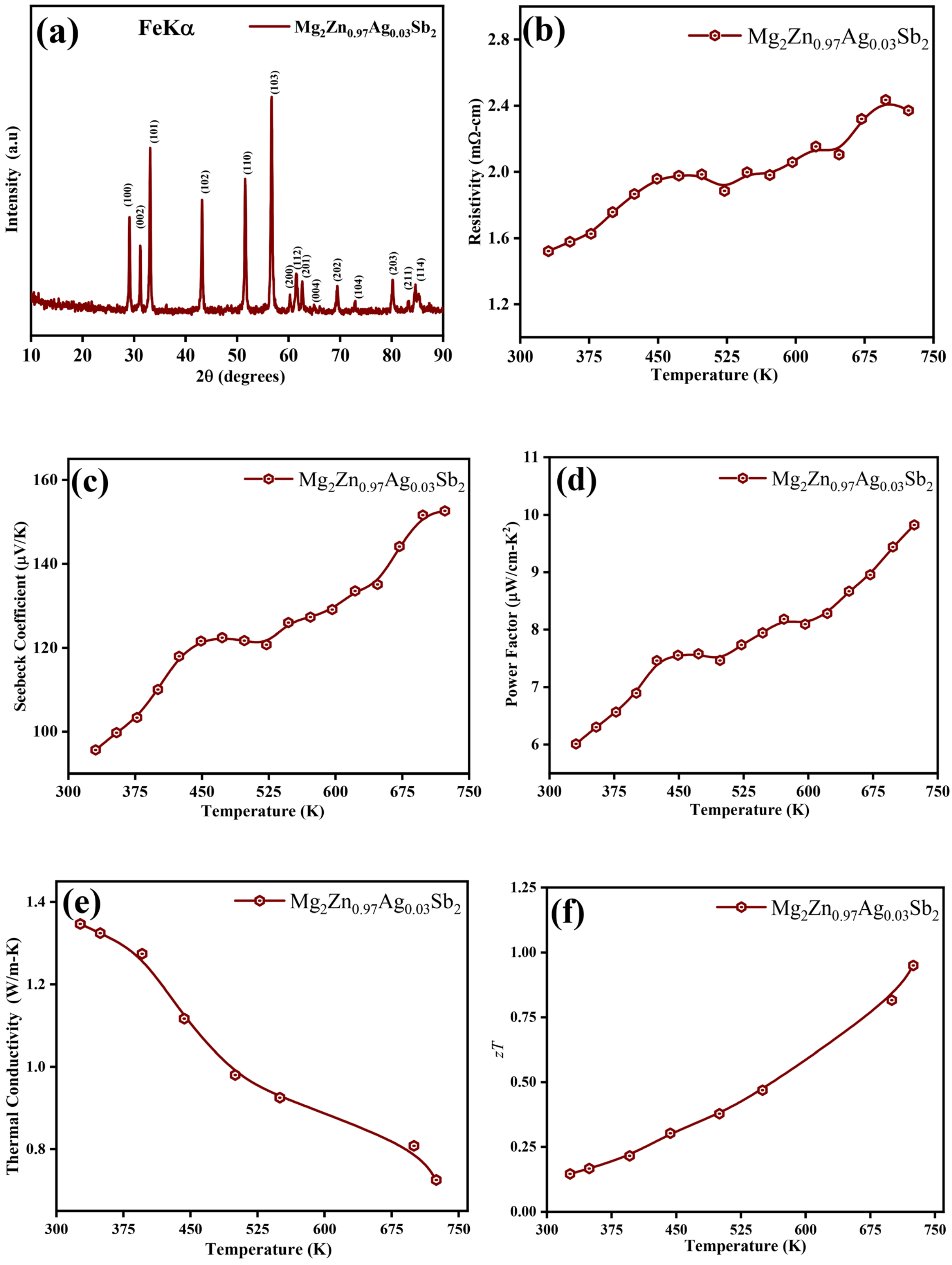

Fig. 14 Structural and thermoelectric characterization of $Mg_2Zn_{0.97}Ag_{0.03}Sb_2$: (a) powder X-ray diffraction pattern, (b) electrical conductivity σ, (c) Seebeck coefficient S, (d) power factor PF, (e) total thermal conductivity κ_{total}, and (f) dimensionless figure of merit zT as functions of temperature.

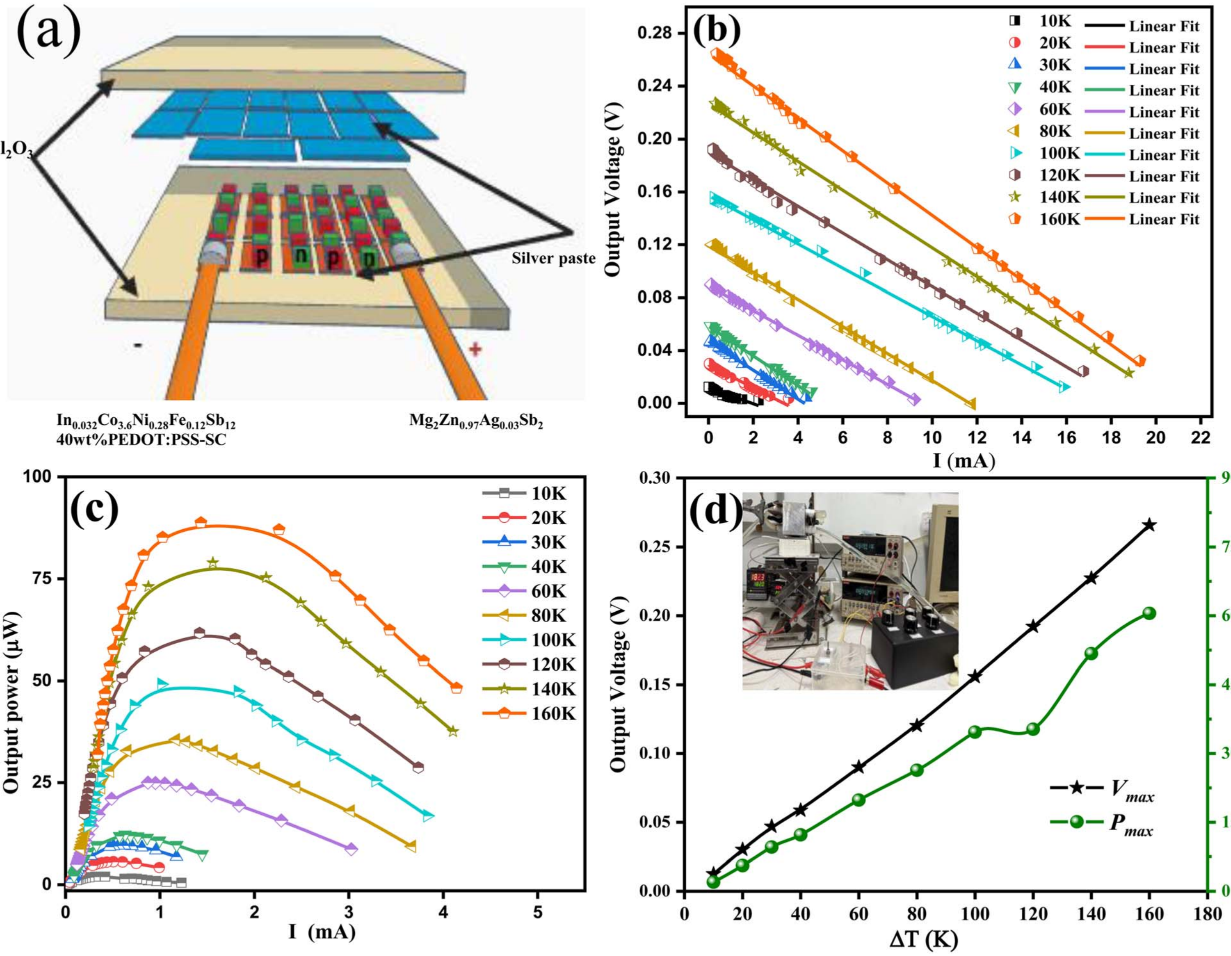

Fig. 15 Thermoelectric generator comprising 10 pairs of p-type $Mg_2Zn_{0.97}Ag_{0.03}Sb_2$ and n-type $In_{0.032}Co_{3.6}Ni_{0.28}Fe_{0.12}Sb_{12}$/40 wt% PEDOT:PSS/S-AC legs: (a) schematic illustration of the device architecture; (b) output voltage *versus* output current at various temperature differences (ΔT); (c) output power *versus* output current at various temperature differences (ΔT); (d) open-circuit voltage (V_{oc}) and maximum output power as a function of ΔT. Inset in (d): photographs of the fabricated TEG and experimental setup.

4. Thermoelectric properties of p-$Mg_2Zn_{0.97}Ag_{0.03}Sb_2$

Fig. 14 shows the XRD patterns and the temperature dependence of the electronic and thermal transport properties of $Mg_2Zn_{0.97}Ag_{0.03}Sb_2$ synthesized by solid-state reaction, followed by evacuated-and-encapsulated sintering and hot-pressing.[9] In Fig. 14(a), the Fe Kα XRD pattern is indexed to the trigonal α-Mg_3Sb_2 structure (ICDD 003-0375) as the major phase, with a minor Sb impurity. Fig. 14(b–f) present the transport properties from 325 to 725 K. The electrical resistivity increases with temperature—rising from 1.52 mΩ cm at 325 K to 2.37 mΩ cm at 725 K—indicative of degenerate-semiconductor behavior. The positive Seebeck coefficient confirms p-type conduction, increasing from 95.6 $\mu V\ K^{-1}$ at 325 K to 152.6 $\mu V\ K^{-1}$ at 725 K. The power factor increases accordingly from 6.01 to 9.82 $\mu W\ cm^{-1}\ K^{-2}$. The total thermal conductivity decreases from 1.34 to 0.72 $W\ m^{-1}\ K^{-1}$. As a result, the dimensionless figure of merit reaches $zT \approx 0.95$ at 725 K.

5. The performance of a thermoelectric generator (TEG) comprising 10 pairs of p-leg $Mg_2Zn_{0.97}Ag_{0.03}Sb_2$ and n-leg $In_{0.032}Co_{3.6}Ni_{0.28}Fe_{0.12}Sb_{12}$ 40 wt% PEDOT:PSS/S-AC

A key design principle for thermoelectric generators is matching the transport properties of the p- and n-legs, including Seebeck coefficient (S), electrical resistivity (ρ), and thermal conductivity (κ), over the intended operating temperature range. Such matching ensures comparable dimensionless figure of merit (zT) and similar optimal current density for both legs, thereby maximizing device efficiency.

In the present work, $Mg_2Zn_{0.97}Ag_{0.03}Sb_2$ was selected as the p-leg because of its high power factor and favorable zT thermoelectric performance in the mid-temperature range. The n-leg was chosen as $In_{0.032}Co_{3.6}Ni_{0.28}Fe_{0.12}Sb_{12}$/40 wt% PEDOT:PSS/S-AC, which exhibits comparable transport

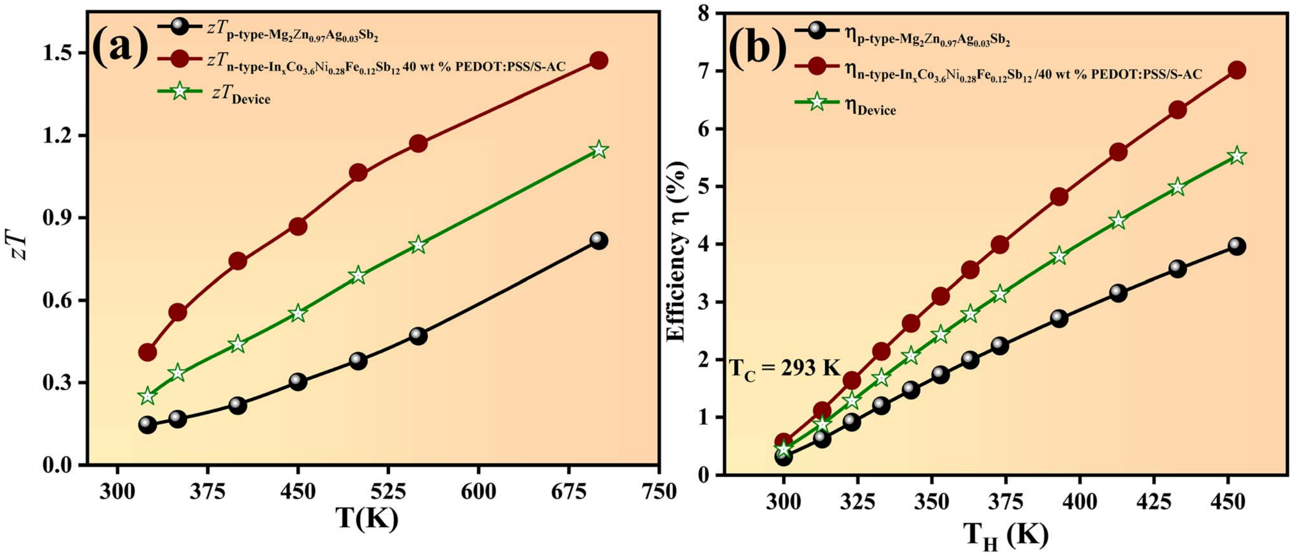

Fig. 16 (a) Temperature dependence of zT for p-leg, n-leg, and the fabricated TEG; (b) temperature dependence of efficiency for p-leg, n-leg, and the fabricated TEG at $\Delta T = 160$ K.

properties within a similar temperature window, making it a suitable counterpart for efficient module operation.

Fig. 15 shows a thermoelectric generator consisting of ten p–n couples fabricated from p-type $Mg_2Zn_{0.97}Ag_{0.03}Sb_2$ and n-type $In_{0.032}Co_{3.6}Ni_{0.28}Fe_{0.12}Sb_{12}$/40 wt% PEDOT:PSS/S-AC composite. The device architecture is illustrated schematically in Fig. 15(a). The current–voltage (I–V) curves measured under different temperature differences (ΔT) are shown in Fig. 15(b). The linear relationship between voltage and current indicates ohmic behavior of the device and is consistent with a Thévenin equivalent source model, in which the output voltage decreases linearly with increasing current.

The output power (P) of the TEG can be expressed as[67]

$$P = \frac{E^2 R_{\text{Load}}}{(R_{\text{internal}} + R_{\text{Load}})^2} \tag{12}$$

where E is the output voltage (mV), R_{Load} (Ω) the load resistance, and R_{internal} (Ω) is the internal resistance of the TEG. As shown in Fig. 15(c), the output power increases with current and reaches a maximum when the load resistance matches the internal resistance of the device ($R_{\text{Load}} = R_{\text{internal}}$). The maximum output power increases progressively with increasing temperature difference, from 1.98 μW at $\Delta T = 10$ K to 5.58, 9.56, 12.24, 25.02, 35.55, 49.19, 61.69, 78.98, and 88.80 μW at $\Delta T = 20$, 30, 40, 60, 80, 100, 120, 140, and 160 K, respectively.

Fig. 15(d) presents the open-circuit voltage (V_{oc}) and maximum output power as a function of temperature difference ($\Delta T = T_H - T_C$). Both quantities increase approximately linearly with ΔT, as expected for thermoelectric modules. At $\Delta T = 160$ K, the open-circuit voltage reaches 0.265 V. Photographs of the fabricated device and the measurement setup are shown in the inset of Fig. 15(d). The output power density was calculated by dividing the maximum output power by the active hot-side area of the module (2.24 mm × 1.91 mm × 10), yielding a maximum value of 203.32 μW cm^{-2} at $\Delta T = 160$ K. The device dimensionless figure of merit for a thermoelectric unicouple operating at temperature T can be estimated using

$$zT_{\text{device}} = \frac{(S_p - S_n)^2 T}{\left[\sqrt{\rho_p k_p} + \sqrt{\rho_n k_n}\right]^2} \tag{13}$$

where S_p and S_n are the Seebeck coefficients for the p- and n-leg, respectively; ρ and κ denote electrical resistivity and thermal conductivity of the constituent materials.[68] At 700 K, the temperature-dependent thermoelectric performance shown in Fig. 16(a) yields $zT_p \approx 0.82$ for the p-leg, $zT_n \approx 1.47$ for the n-leg, and an estimated $zT_{\text{device}} \approx 1.15$ for the module.

The ideal conversion efficiency η, assuming a temperature-independent average zT, can be estimated using[68]

$$\eta = \frac{T_H - T_C}{T_H} \frac{\sqrt{1 + zT} - 1}{\sqrt{1 + zT} + \dfrac{T_C}{T_H}} \tag{14}$$

where zT represents the dimensionless figure of merit, T_H the hot side temperature, and T_C the cold side temperature.[68] As shown in Fig. 16(b), when T_C is fixed at 293 K and T_H varies from 303 to 453 K ($\Delta T = 10$–160 K), the calculated maximum efficiencies reach 3.96% (p-leg), 7.01% (n-leg), and 5.53% (module) at $\Delta T = 160$ K.

To better contextualize the performance of the present device, Table 2 compares the output power density and efficiency of the fabricated module with representative skutterudite-based thermoelectric generators reported in the literature. As summarized in Table 2, previously reported skutterudite modules typically operate under substantially larger temperature differences ($\Delta T \approx 366$–673 K), whereas the present module delivers competitive power density under a relatively moderate temperature gradient. This comparison highlights the effectiveness of the present material combination and device architecture for thermoelectric power generation under moderate operating conditions.

Table 2 Comparison of the thermoelectric module performance of the present work with representative skutterudite-based thermoelectric generators reported in the literature, including material systems, number of thermoelectric pairs, module configuration, operating temperature difference (ΔT), power density, power output, and conversion efficiency

Material								
P-leg	N-leg	No. of pairs	TEG	ΔT (K)	Power density	Power output	η (%)	Ref.
$Ce_{0.45}Co_{2.5}Fe_{1.5}Sb_{12}$	$Yb_{0.25}Co_4Sb_{12}/Yb_2O_3$	2	Bulk	490	N/A	140 mW	6.4	69
$CoSb_3$	$CoSb_{2.85}Te_{0.15}$	4	Bulk (Tubular)	425	0.52 Wcm^{-2}	[a]	[a]	70
$DD_yFe_3CoSb_{12}$	$(Mm, Sm)_yCo_4Sb_{12}$	8	Bulk	570	2.1 W cm^{-2}	8.06 W	[a]	71
$Ce_{0.85}Fe_3CoSb_{12}$/1.4 vol% rGO	$Yb_{0.27}Co_4Sb_{12}$/0.72 vol% rGO	8	Bulk	577	[a]	3.8 W	8.4	72
$CeFe_3CoSb_{12}$	$Yb_{0.15}CoSb_{12}$	14	Bulk	580	3.54 kW m^{-2}	2.43 W	[a]	73
$NdFe_{3.5}Co_{0.5}Sb_{12}$	$Yb_{0.35}Co_4Sb_{12}$	1	Bulk	480	[a]	[a]	9.1	74
$La_{0.7}Ti_{0.1}Ga_{0.1}Fe_{2.7}Co_{1.3}Sb_{12}$	$Yb_{0.25}Fe_{0.25}Co_{3.75}Sb_{12}$	1	Bulk	366	[a]	336.7 mW	7.27	75
$CeFe_{3.5}Co_{0.5}Sb_{12}$	$CoSb_3$	1	Bulk	673	[a]	0.67 W	10.7	76
$In_{0.25}Co_3FeSb_{12}$	$In_{0.25}Co_{3.95}Ni_{0.05}Sb_{12}$	1	Bulk	543	[a]	796 mW	[a]	77
$(La, Ba, Ga, Ti)_{0.9}Fe_3CoSb_{12}$	$(Yb, Ca, Al, Ga, In)_{0.7}Fe_{0.25}Co_{3.75}Sb_{12}$	32	Bulk	550	[a]	25 W	7.2	78
$Mg_2Zn_{0.97}Ag_{0.03}Sb_2$	$In_{0.032}Co_{3.6}Ni_{0.28}Fe_{0.12}Sb_{12}$ 40 wt% PEDOT:PSS/S-AC	10	Bulk	160	203.32 μW cm^{-2}	88.80 μW	5.53	This work

[a] Not given.

6. Conclusion

This study demonstrates a hybrid materials design that simultaneously enhances electronic transport and suppresses lattice heat flow in filled skutterudites. During bulk co-processing, HNO_3-treated PEDOT:PSS transforms into sulfur-rich amorphous carbon (S-AC) interphases that, together with In filling, generate a hierarchical micro/mesoporous network throughout the ceramic matrix. This topology introduces multiple scattering pathways that extend beyond the influence of porosity alone: diffuse Casimir/Knudsen boundary scattering at pore walls and intergranular layers, pronounced acoustic and vibrational-spectrum mismatch across amorphous S-AC interfaces, and mass/strain-field fluctuations associated with finely dispersed InSb/Sb nanophases. Collectively, these interface-dominated processes produce a level of κ_L suppression that is stronger than typically expected from dilute-porosity behavior and characteristic of hybrid systems where amorphous interphases play a central transport-modifying role.

On the electronic side, analysis using a Kane-model Lorenz number reveals a composition-dependent balance between improved intergrain connectivity and interphase-induced scattering. Moderate polymer loadings enhance mobility-weighted conductivity and raise κ_e, whereas high interphase density introduces extensive carrier scattering that reduces both κ_e and resistivity-derived transport benefits. This crossover yields the lowest κ_T and highest thermoelectric performance at elevated temperatures. The optimal composite achieves $zT = 1.47$ at 700 K with $\kappa \approx 0.74$ W m^{-1} K^{-1}, and a 10-pair module output of 203 μW cm^{-2} at 5.53% efficiency under $\Delta T = 160$ K, underscoring the practical viability of the approach.

Because both the interphase chemistry and pore architecture are tunable through polymer loading and processing conditions, this polymer-to-S-AC transformation provides a generalizable strategy for engineering interface-dominated phonon scattering in mid-temperature thermoelectrics. Future efforts combining pore-size statistics, interfacial thermal resistance measurements, and mean-free-path-resolved modeling will enable predictive design rules and more universal guidelines for integrating amorphous interphases into high-performance thermoelectric materials and devices.

Conflicts of interest

There are no conflicts of interest to declare.

Data availability

All data supporting the findings of this study are available within the article and its supplementary information (SI). Additional raw data that support the findings are available from author upon request. Supplementary information: additional characterization data, including Rietveld refinement analysis, FE-SEM elemental mapping, HRTEM analysis, Hall carrier concentration and mobility plots, and tables. See DOI: https://doi.org/10.1039/d6ta00685j.

Acknowledgements

This work was supported by the National Science and Technology Council of Taiwan under Grant No. 114-2112-M-018-004.

References

1 G. J. Snyder and E. S. Toberer, *Nat. Mater.*, 2008, **7**, 105–114.
2 A. Gharleghi, T.-Z. Wei and C.-J. Liu, *ACS Appl. Energy Mater.*, 2024, 7, 10738–10749.
3 J. E. Ni, E. D. Case, K. N. Khabir, R. C. Stewart, C.-I. Wu, T. P. Hogan, E. J. Timm, S. N. Girard and M. G. Kanatzidis, *Mater. Sci. Eng., B*, 2010, **170**, 58–66.
4 A. R. Muchtar, B. Srinivasan, S. L. Tonquesse, S. Singh, N. Soelami, B. Yuliarto, D. Berthebaud and T. Mori, *Adv. Energy Mater.*, 2021, **11**, 2101122.
5 B. Srinivasan, S. Le Tonquesse, A. Gellé, C. Bourgès, L. Monier, I. Ohkubo, J.-F. Halet, D. Berthebaud and T. Mori, *J. Mater. Chem. A*, 2020, **8**, 19805–19821.
6 W.-H. Chen, Z.-R. Yang, F.-H. Lin and C.-J. Liu, *J. Mater. Sci.*, 2017, **52**, 9728–9738.
7 A. Ahmad and C.-J. Liu, *Phys. Chem. Chem. Phys.*, 2023, **25**, 16587–16596.
8 V. P. Kannan, V. Lourdhusamy, I. Paulraj, C.-J. Liu and S. Madanagurusamy, *ACS Appl. Mater. Interfaces*, 2023, **15**, 47058–47069.
9 V. P. Kannan, V. Lourdhusamy, I. Paulraj, S. Madanagurusamy and C.-J. Liu, *ACS Appl. Mater. Interfaces*, 2024, **16**, 58677–58688.
10 I. Paulraj, V. Lourdhusamy and C.-J. Liu, *Chem. Eng. J.*, 2022, **446**, 137083.
11 R. B. Smriti, W. Li, A. Nozariasbmarz, S. Ghosh, N. Liu, C. D. Rahn, M. Sanghadasa, S. Priya and B. Poudel, *ACS Appl. Mater. Interfaces*, 2025, **17**, 4904–4912.
12 A. Gharleghi, Y. Liu, M. Zhou, J. He, T. M. Tritt and C.-J. Liu, *J. Mater. Chem. A*, 2016, **4**, 13874–13880.
13 A. Gharleghi and C.-J. Liu, *J. Alloys Compd.*, 2014, **592**, 277–282.
14 Z.-H. Zheng, J.-Y. Niu, D.-W. Ao, B. Jabar, X.-L. Shi, X.-R. Li, F. Li, G.-X. Liang, Y.-X. Chen and Z.-G. Chen, *J. Mater. Sci. Technol.*, 2021, **92**, 178–185.
15 C. Bourgès, W. Zhang, K. K. Raut, Y. Owada, N. Kawamoto, M. Mitome, K. Kobayashi, J.-F. Halet, D. Berthebaud and T. Mori, *ACS Appl. Energy Mater.*, 2023, **6**, 9646–9656.
16 D. Li, X. L. Shi, J. Zhu, M. Li, J. Wang, W. D. Liu, Q. Zhao, H. Zhong, S. Li and Z. G. Chen, *Adv. Energy Mater.*, 2023, **13**, 2301525.
17 Z. Liu, Y. Wang, T. Yang, Z. Ma, H. Zhang, H. Li and A. Xia, *J. Adv. Ceram.*, 2023, **12**, 539–552.
18 Q. Zhang, B. Liao, Y. Lan, K. Lukas, W. Liu, K. Esfarjani, C. Opeil, D. Broido, G. Chen and Z. Ren, *Proc. Natl. Acad. Sci. U. S. A.*, 2013, **110**, 13261–13266.
19 Y.-L. Pei, H. Wu, D. Wu, F. Zheng and J. He, *J. Am. Chem. Soc.*, 2014, **136**, 13902–13908.
20 D. Li, X. L. Shi, Z. Feng, M. Li, J. Zhu, X. Ma, L. Zhang, H. Zhong, W. D. Liu and S. Li, *Adv. Funct. Mater.*, 2023, **33**, 2305269.
21 V. Trivedi, M. Tiadi, B. S. Murty, D. K. Satapathy, M. Battabyal and R. Gopalan, *ACS Appl. Mater. Interfaces*, 2022, **14**, 51084–51095.
22 X. Meng, Z. Liu, B. Cui, D. Qin, H. Geng, W. Cai, L. Fu, J. He, Z. Ren and J. Sui, *Adv. Energy Mater.*, 2017, **7**, 1602582.
23 K. Biswas, J. He, I. D. Blum, C.-I. Wu, T. P. Hogan, D. N. Seidman, V. P. Dravid and M. G. Kanatzidis, *Nature*, 2012, **489**, 414–418.
24 A. Gharleghi, P.-C. Hung, F.-H. Lin and C.-J. Liu, *ACS Appl. Mater. Interfaces*, 2016, **8**, 35123–35131.
25 A. Gharleghi, Y.-H. Chu, F.-H. Lin, Z.-R. Yang, Y.-H. Pai and C.-J. Liu, *ACS Appl. Mater. Interfaces*, 2016, **8**, 5205–5215.
26 S.-J. Jung, J. Shin, S.-S. Lim, B. Kwon, S.-H. Baek, S. K. Kim, H.-H. Park and J.-S. Kim, *Nano Energy*, 2021, **81**, 105604.
27 D. B. S. Sethuraman, Y.-C. Chen and C.-J. Liu, *J. Mater. Chem. A*, 2025, **13**, 36609–36631.
28 I. Paulraj, V. Lourdhusamy, A. Niranjan and C.-J. Liu, *Chem. Eng. J.*, 2025, **525**, 170262.
29 I. Paulraj, V. Lourdhusamy and C.-J. Liu, *ACS Appl. Energy Mater.*, 2025, **8**, 12177–12189.
30 A. Gharleghi, Y.-H. Pai, F.-H. Lin and C.-J. Liu, *J. Mater. Chem. C*, 2014, **2**, 4213–4220.
31 H. Sun, X. Jia, P. Lv, L. Deng, X. Guo, Y. Zhang, B. Sun, B. Liu and H. Ma, *RSC Adv.*, 2015, **5**, 61324–61329.
32 A. Ivanova, A. Novitskii, I. Serhiienko, G. Guélou, T. Sviridova, S. Novikov, M. Gorshenkov, A. Bogach, A. Korotitskiy and A. Voronin, *J. Mater. Chem. A*, 2023, **11**, 2334–2342.
33 Z.-Y. Liu, J.-L. Zhu, X. Tong, S. Niu and W.-Y. Zhao, *J. Adv. Ceram.*, 2020, **9**, 647–673.
34 V. Lourdhusamy, J.-L. Chen, I. Paulraj, L.-C. Hsu, Y.-Y. Li, T.-S. Yang, K. V. Prabu and C.-J. Liu, *J. Alloys Compd.*, 2022, **920**, 165949.
35 V. N. M. Mani Arockia Doss, J. P. Isaqu, V. Lourdhusamy, Y.-W. Lin and L. Horng, *J. Energy Storage*, 2026, **151**, 120459.
36 B. Jiang, Y. Liu, J. Zhang, Y. Wang, X. Zhang, R. Zhang, L.-L. Huang and D. Zhang, *RSC Adv.*, 2022, **12**, 1471–1478.
37 Z. M. Detweiler, S. M. Wulfsberg, M. G. Frith, A. B. Bocarsly and S. L. Bernasek, *Surf. Sci.*, 2016, **648**, 188–195.
38 R. Xu, K. Xu, Y. Sun, Y. Wen, L. Cheng, F.-c. Shen and Y. Qian, *Nanoscale*, 2023, **15**, 18473–18480.
39 A. Graf, M. Isaacs and D. Morgan, *Surf. Interface Anal.*, 2026, **58**, 89–95.
40 T. Islam, S. Chandra Roy, S. Bayat, M. Adigo Weret, J. M. Hoffman, K. R. Rao, C. Sawicki, J. Nie, R. Alam and O. Oketola, *ChemSusChem*, 2024, **17**, e202400084.
41 A. K. Nayak, S. Lee, Y. Sohn and D. Pradhan, *CrystEngComm*, 2014, **16**, 8064–8072.
42 S. T. Jackson and R. G. Nuzzo, *Appl. Surf. Sci.*, 1995, **90**, 195–203.
43 C. Guan, Z. Wu, S. Zhang, Z. Zhao, X. Zhao, Y. Tian, L. Shi and X. Feng, *J. Mater. Sci. Mater. Electron.*, 2023, **34**, 243.
44 Y. Fan, T. Wang, R. Asrosa, B. Li, N. Naresh, X. Liu, S. Guan, R. Li, M. Wang and I. P. Parkin, *Chem. Eng. J.*, 2024, **488**, 150672.
45 W. Li, Z. Yu, C. Liu, Y. Peng, B. Feng, J. Gao, G. Wu, X. Bai, J. Chen and X. Wang, *J. Adv. Ceram.*, 2023, **12**, 1511–1520.

46 C. Liu, Z. Zhang, Y. Peng, F. Li, L. Miao, E. Nishibori, R. Chetty, X. Bai, R. Si and J. Gao, *Sci. Adv.*, 2023, **9**, eadh0713.

47 I. Forero-Sandoval, A. Franco-Bacca, F. Cervantes-Álvarez, C. Gómez-Heredia, J. Ramírez-Rincón, J. Ordonez-Miranda and J. Alvarado-Gil, *J. Appl. Phys.*, 2022, **131**, 230901.

48 I. Paulraj, V. Lourdhusamy, Z.-R. Yang, C.-H. Wang and C.-J. Liu, *J. Power Sources*, 2023, **572**, 233096.

49 G. J. Snyder, A. Pereyra and R. Gurunathan, *Adv. Funct. Mater.*, 2022, **32**, 2112772.

50 A. Bhaskar, Y.-W. Yang, Z.-R. Yang, F.-H. Lin and C.-J. Liu, *Ceram. Int.*, 2015, **41**, 7989–7995.

51 F.-H. Lin and C.-J. Liu, *Sci. Rep.*, 2022, **12**, 7056.

52 A. Bhardwaj, A. Shukla, S. Dhakate and D. Misra, *RSC Adv.*, 2015, **5**, 11058–11070.

53 C.-W. Nan, R. Birringer, D. R. Clarke and H. Gleiter, *J. Appl. Phys.*, 1997, **81**, 6692–6699.

54 Y. Cao, T. Zhu and X. Zhao, *J. Phys. D: Appl. Phys.*, 2008, **42**, 015406.

55 D. G. Cahill, W. K. Ford, K. E. Goodson, G. D. Mahan, A. Majumdar, H. J. Maris, R. Merlin and S. R. Phillpot, *J. Appl. Phys.*, 2003, **93**, 793–818.

56 H. Casimir, *Physica*, 1938, **5**, 495–500.

57 J. M. Ziman, *Electrons and Phonons: The Theory of Transport Phenomena in Solids*, Oxford Univ. Press, 2001.

58 V. D. Bruggeman, *Ann. Phys.*, 1935, **416**, 636–664.

59 D. McLachlan, *J. Phys. C: Solid State Phys.*, 1987, **20**, 865.

60 V. Lourdhusamy, I. Paulraj, V. P. Kannan and C.-J. Liu, *J. Mater. Chem. A*, 2025, **13**, 6027–6041.

61 I. Paulraj, V. Lourdhusamy and C.-J. Liu, *Mater. Sci. Semicond. Process.*, 2025, **188**, 109252.

62 S. S. S. Gadhavajhala, V. P. Kannan, A. J. Kale, R. Batra, S. R. Mishra and B. Srinivasan, *Small*, 2025, **21**, 2411481.

63 R. Viennois, T. Kume, M. Komura, L. Girard, A. Haidoux, J. Rouquette and M. Koza, *J. Phys. Chem. C*, 2020, **124**, 23004–23012.

64 R. Rubio-Govea, A. Opis-Basilio, A. Torres, M. Sánchez, K. Ray and K. A. Mazzio, *J. Phys. Chem. C*, 2024, **128**, 18612–18621.

65 S. Matsushita, B. Yan, T. Matsui, J.-D. Kim and K. Akagi, *RSC Adv.*, 2018, **8**, 19512–19523.

66 R. Cuscó, E. Alarcón-Lladó, J. Ibáñez, L. Artús, J. Jiménez, B. Wang and M. J. Callahan, *Phys. Rev. B*, 2007, **75**, 165202.

67 V. Lourdhusamy, I. Paulraj and C.-J. Liu, *Inorg. Chem.*, 2024, **63**, 3735–3748.

68 V. Karthikeyan, J. U. Surjadi, J. C. Wong, V. Kannan, K.-H. Lam, X. Chen, Y. Lu and V. A. Roy, *J. Power Sources*, 2020, **455**, 227983.

69 D. Zhao, C. Tian, S. Tang, Y. Liu, L. Jiang and L. Chen, *Mater. Sci. Semicond. Process.*, 2010, **13**, 221–224.

70 H. Jang, J. B. Kim, A. Stanley, S. Lee, Y. Kim, S. H. Park and M.-W. Oh, *Energies*, 2020, **13**, 1106.

71 S. H. Park, Y. Jin, J. Cha, K. Hong, Y. Kim, H. Yoon, C.-Y. Yoo and I. Chung, *ACS Appl. Energy Mater.*, 2018, **1**, 1603–1611.

72 P.-A. Zong, R. Hanus, M. Dylla, Y. Tang, J. Liao, Q. Zhang, G. J. Snyder and L. Chen, *Energy Environ. Sci.*, 2017, **10**, 183–191.

73 S. Katsuyama, W. Yamakawa, Y. Matsumura and R. Funahashi, *J. Electron. Mater.*, 2019, **48**, 5257–5263.

74 A. Muto, J. Yang, B. Poudel, Z. Ren and G. Chen, *Adv. Energy Mater.*, 2013, **3**, 245–251.

75 W. Li, D. Stokes, B. Poudel, U. Saparamadu, A. Nozariasbmarz, H. B. Kang and S. Priya, *Energies*, 2019, **12**, 4292.

76 H. H. Saber, M. S. El-Genk and T. Caillat, *Energy Convers. Manag.*, 2007, **48**, 555–567.

77 S.-M. Choi, K.-H. Kim, S.-M. Jeong, H.-S. Choi, Y. S. Lim, W.-S. Seo and I.-H. Kim, *J. Electron. Mater.*, 2012, **41**, 1004–1010.

78 G. Nie, S. Suzuki, T. Tomida, A. Sumiyoshi, T. Ochi, K. Mukaiyama, M. Kikuchi, J. Guo, A. Yamamoto and H. Obara, *J. Electron. Mater.*, 2017, **46**, 2640–2644.